Forward and backward propagating breathers in a DNA model with dipole-dipole long-range interactions

Carlos Lawrence Gninzanlong,[1,*] Frank Thomas Ndjomatchoua,[2,†] and Clément Tchawoua[1,‡]
[1]*Department of Physics, Faculty of Science, University of Yaoundé 1, P.O. Box 812, Yaoundé, Cameroon*
[2]*Geospatial Science & Modelling Cluster, Sustainable Impact Platform, International Rice Research Institute (IRRI), DAPO Box 7777-1301, Metro Manila, Philippines*

(Received 18 July 2019; revised 4 September 2020; accepted 29 October 2020; published 20 November 2020)

The present study explores the existence and orbital stability of discrete bright breathers through the Joyeux-Buyukdagli DNA model incorporating long-range interactions (LRIs). The nonlinear Schrödinger equation is derived from a semidiscrete approximation and subsequently used to construct the targeted initial condition for numerical computations of the discrete breather. It appears that the interplay between the carrier wave frequency and the LRI induces stationary forward or backward propagating waves. For critical values of the LRI, stationary waves can occur out of the center/edge of the first Brillouin zone. The predicted breathers differ in their robustness and mobility for specific carrier-wave frequency and LRI. In all cases, semianalytical predictions agree with numerical simulations.

DOI: 10.1103/PhysRevE.102.052212

I. INTRODUCTION

In physics it is now commonly accepted that, without a break of translational invariance by an impurity or disorder, energy localization can occur in a system under the form of an intrinsic localized mode solely due to nonlinearity [1–4]. The discrete breather (DB) [also termed the intrinsic localized mode (ILM)] is a solution that is spatially localized as well as temporally periodic in a spatially discrete system [1–4]. DBs have been extensively studied numerically and experimentally in various practical nonlinear systems [1–4]. Although they have the propensity to be strongly pinned at a specific location of the lattice, they can also move easily under some circumstances while maintaining their localization [5,6]. Although DBs are mainly investigated in short-range lattice systems having, typically, nearest-neighbor interaction [1–4], they are also observed in next-nearest-neighbor interacting systems [7–9]. Another family, termed long-range interacting systems, can also form lattice structures such as Fermi-Pasta-Ulam systems [10–12], vortices of plasmas [13,14], a photonic crystal waveguide [15,16], fluids [17], a magnetic chain [18], and DNA [19–25].

The DNA molecule belongs to the class of biopolymers, and it has a very important biological function. It supports genetic information and allows the transmission of this information from cell to cell and from one generation to another via replication and transcription or recombination processes [26–28]. It is a biomolecule in which nonlinearity, localization, and energy transfer emerge as prevailing regulatory factors [27,28]. It is also an appealing playground to study the effect of long-range forces, because the hydrogen bond responsible for the DNA interbase coupling has a finite dipole moment and produces long-range interaction (LRI) forces [19–25]. Most of the nonlinear wave studies of LRI in DNA are based on the Peyrard-Bishop (PB) model [19–25]. The PB model was refined by Joyeux and Buyukdagli (JB) to have phase-transition curves in agreement with experimental observations and to ensure a sharp melting transition [29,30]. The nonlinear DNA model developed by JB was previously used to study quasicontinuum compactons, fractional breathers, and DBs without LRI [31–35]. Therefore, in order to deal with a more realistic DNA model, a modified version of the JB model including LRI is selected as the core model in this study.

Nonlinear models can correctly predict the regions where a DNA molecule is more likely to open [36]. In addition, breathing modes that can be evidenced analytically/numerically through such models are presently widely accepted to be at the initiation of transcription in DNA [27,28]. This biomolecule has thus drawn considerable interest in the community of nonlinear physicists [19–25,27–35].

There are two dominant pictures for the computational studies of breathing mode dynamics in DNA. The first one uses the low amplitude and weakly nonlinear approximation in order to get the nonlinear Schrödinger (NLS) equation and to estimate the breather solution [27,28]. Although this quasicontinuum multiscale approximation appears to provide an analytically tractable wave amplitude profile [27,28], this continuum of initial breathers is unstable compared to its discrete analog [37]. The second picture shows how to compute the exact solution numerically starting with a chosen initial condition from the anticontinuous limit (i.e., the solution of the uncoupled lattice dynamics), and "*continue*" it using the Newton-Raphson method up to some specified value of the neighbor coupling constant [19–21,25]. Both approaches have considerable challenges: (i) the solution of the first picture is

*gcarloslawrence@yahoo.fr
†ftndjomatchoua@gmail.com
‡ctchawa@yahoo.fr

quasidiscrete, though the real DNA is discrete; (ii) the finding of the solution during the estimate of the discrete analog with the second picture is somewhat challenging due to numerous possibilities to select the initial spatial configuration for numerical computation of the exact DB after obtaining the anticontinuous solution. To overcome the previously mentioned challenges, the procedure for estimating the DB in this study begins with the standard NLS-model reduction to identify the initial *ansatz* analytically and then subsequently estimate the true nonlinear DB solutions numerically [38–40]. To the best of our knowledge, this has yet to be done in the study of nonlinear lattices with LRI [10–14,17–25,41,42].

In the past decade, it was demonstrated that a decrease in the carrier wave frequency in the first Brillouin zone induces a negative sign of the group velocity and can subsequently lead to the emergence of backward wave propagation [38,43–45]. It was further demonstrated that backward or forward waves can be obtained just by varying a system parameter without changing the overall system structure; this is termed chameleon behavior (CB) [46]. Although the study of nonlinear dynamics and solitons in LRI systems was first conducted several decades ago (e.g., Tchawoua *et al.* [47] and Remoissenet *et al.* [48]), and more recently (e.g., [10–14,17–25,41,42]), to best of our knowledge the CB has yet to be reported in LRI models. The present study explored the possibility of observing CB in a LRI system as well as analyzing breather orbital stability.

Following the Introduction (Sec. I), the rest of the present paper is structured as follows: In Sec. II, the model object of our study is introduced. It is a modification of the JB DNA model [29,30], with the incorporation of a LRI term due to dipole-dipole interactions. After derivation of the lattice-dynamics equations, the semidiscrete approximation is applied, the NLS equation is derived and the approximate analytical solution is obtained. In Sec. III, the DB is obtained and its stability is verified. Following Cuevas *et al.* [19–22], the effect of the LRI variation of the DNA model is systematically investigated while conducting an analysis. In Sec. IV, the obtained results are discussed, and the study ends with a summary and concluding remarks (Sec. V).

II. THE MODEL

The version of the JB model considered here consists of adding an energy term to the original Hamiltonian [29,30] that takes into account LRI due to the dipole-dipole forces. The Hamiltonian of the JB model can be rewritten as

$$\begin{aligned} H &= \sum_n H_n, \\ H_n &= \frac{1}{2m}P_n^2 + D[1-\exp(-ay_n)]^2 \\ &\quad + \frac{\Delta H}{C_J}\left[1-\exp\left(-b(y_n-y_{n-1})^2\right)\right] + K_b(y_n-y_{n-1})^2 \\ &\quad + \frac{1}{2}\sum_{\kappa\neq n}\frac{q^2}{4\pi\varepsilon_0 d^3}\frac{1}{|\kappa|^3}y_{n+\kappa}y_n. \end{aligned} \tag{1}$$

This Hamiltonian corresponds to the case of a homogeneous DNA molecule in which dipole moments are parallels and point all in the same direction. In Eq. (1), $P_n = m\dot{y}_n$ is the momentum, y_n represents the transverse stretching of the nucleotide pair at site n, and m denotes the mass of a nucleotide. The variables D and a are, respectively, the depth and inverse width of the Morse potential, ΔH is a finite stacking energy, b is the spatial scale factor, and K_b is a harmonic elastic constant. The last term (LRI) in Eq. (1), which was not considered in the JB model [29,30], has the following coefficients: d is the distance between consecutive neighboring base pairs in the same strand, and q is the charge transfer due to the stretching of hydrogen bonds [19–22]. The LRI is limited to $(N-1)/2$ neighboring base pairs if N is odd or to $(N-2)/2$ neighboring base pairs in each direction of a given site of the chain if N is even [19–22]. The dimensionless equation of motion corresponding to the Hamiltonian Eq. (1) is

$$\begin{aligned} &\frac{d^2Y_n}{d\tau^2} + \frac{2K_b}{a^2D}(2Y_n - Y_{n+1} - Y_{n-1}) \\ &\quad + \frac{1}{a^2D}\sum_{\kappa\neq n} J_\kappa Y_{n+\kappa} \\ &\quad + \frac{2b\Delta H}{a^2DC_J}\left[(Y_n - Y_{n-1})e^{-\frac{b}{a^2}(Y_n-Y_{n-1})^2}\right] \\ &\quad - \frac{2b\Delta H}{a^2DC_J}\left[(Y_{n+1} - Y_n)e^{-\frac{b}{a^2}(Y_{n+1}-Y_n)^2}\right] \\ &\quad - 2\left(e^{-Y_n}-1\right)e^{-Y_n} = 0, \end{aligned} \tag{2}$$

where $Y_n = ay_n$, $\tau = t\sqrt{a^2D/m}$, and $J_\kappa = \frac{q^2}{4\pi\varepsilon_0 d^3|\kappa|^3}$. The coupling constant J_κ is related to the charge transfer due to the formation of the hydrogen bonds (q) and the distance between base pairs (d). The subscript κ is the normalized distance between base pairs [19–22].

Following the original approach in [49], it is assumed that the oscillations of bases are large enough to be anharmonic, but still insufficient to break the bond since the plateau of the Morse potential is not reached. It is then presumed that the base nucleotides oscillate around the bottom of the Morse potential. On the one hand, the wave amplitude is considered large enough, so that the nonlinear effects that play an essential role in the DNA dynamics can be incorporated [27,28]. On the other hand, it is still very small compared with the motions that result in permanently open states where the nucleotides reach the plateau of the Morse potential. We can therefore expand the terms $\exp[-\frac{b}{a^2}(Y_{n\pm1}-Y_n)^2]$ and $\exp[-Y_n]$ in Eq. (2) up to second and third order, respectively [31–35]. The corresponding equation of motion is

$$\begin{aligned} &\ddot{Y}_n - k_2(Y_{n+1} - 2Y_n + Y_{n-1}) + \omega_g^2\left(Y_n - \alpha Y_n^2 + \beta Y_n^3\right) \\ &\quad + k_4\left[(Y_{n+1}-Y_n)^3 - (Y_n - Y_{n-1})^3\right] \\ &\quad + \sum_\kappa \hat{J}_\kappa Y_{n+\kappa} = 0, \end{aligned} \tag{3}$$

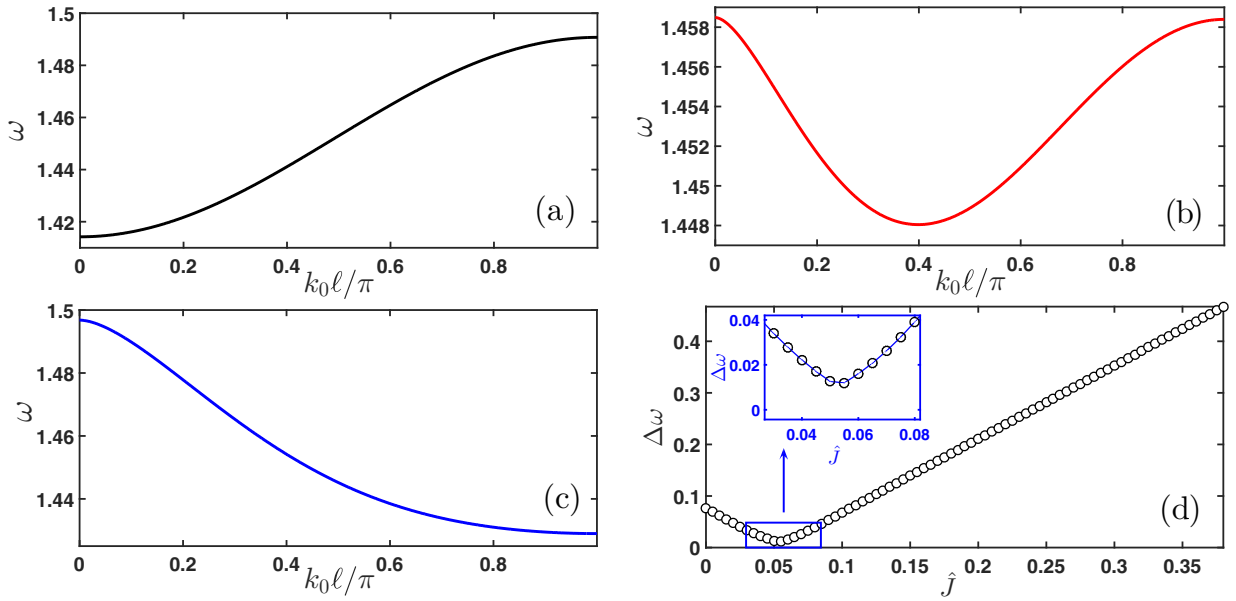

FIG. 1. The linear dispersion relation showing the pulsation ω as a function of the wave number k_0 in the first Brillouin zone for different values of $\hat{J}$: (a) $\hat{J} = 0$, (b) $\hat{J} = 0.053$, and (c) $\hat{J} = 0.1$. (d) Variation of the allowed phonon band according to $\hat{J}$.

with the coefficients

$$k_2 = \frac{2}{a^2 D}\left(K_b + \frac{b\Delta H}{C_J}\right), \quad k_4 = \frac{2\Delta H b^2}{C_J D a^4}, \quad \omega_g^2 = 2,$$
$$\hat{J}_\kappa = \begin{cases} \frac{\hat{J}}{|\kappa|^3} & \text{for} \quad 1 \leqslant |\kappa| \leqslant (N-1)/2, \\ 0 & \text{otherwise}, \end{cases} \qquad \alpha = \frac{3}{2}, \qquad (4)$$
$$\beta = \frac{7}{6}, \quad \hat{J} = \frac{q^2}{4\pi\varepsilon_0 a^2 d^3 D},$$

where $|\kappa|$ is the normalized distance between base pairs. The used parameters are $m = 300$ amu, $D = 0.04$ eV, $a = 4.45$ Å^{-1}, $b = 0.10$ Å^{-2}, $\Delta H = 0.44$ eV, $K_b = 10^{-5}$ eV Å^{-2}, $d = 3.4$ Å, $\varepsilon_0 = 8.85 \times 10^{-12}$ Fm^{-1}, and $C_J = 2$ [19–22,29,30].

A. Linear analysis

By keeping only linear terms in Eq. (3), a plane-wave solution is assumed in the form $Y_n(\tau) = A\exp[i(k_0 n\ell - \omega\tau)]$, where A is the constant amplitude, ℓ is the distance separating neighboring bases, and ω and k_0 denote the angular frequency and the wave number, respectively. The substitution of the previously mentioned plane-wave ansatz into Eq. (3) leads to the following linear dispersion relation:

$$\omega^2 = \omega_g^2 + 4k_2 \sin^2\left(\frac{k_0\ell}{2}\right) + 2\hat{J}\sum_m \frac{\cos(k_0 m\ell)}{m^3}. \qquad (5)$$

By using Eq. (5), the angular frequency ω is plotted as a function of the wave number k_0 in the first Brillouin zone ($k_0 \in [0, \pi/\ell]$ [50]) for three different values of $\hat{J}$ (see Fig. 1). It can be noticed that the dipole-dipole coupling constant prominently shapes the regions for the allowed/forbidden band-gap frequencies. For certain values of $\hat{J}$, the dispersion curve has a positive [Fig. 1(a)], a negative [Fig. 1(c)], or a mixed [Fig. 1(b)] slope. As the group velocity (v_g) of the wave is linked with the dispersion relation, the sign of the slope of the dispersion curve gives an indication about the sign of v_g. From Eq. (5), the group velocity is derived as follows:

$$v_g \equiv \frac{\partial\omega}{\partial k_0} = \frac{1}{\omega}\left[k_2\ell\sin(k_0\ell) - \hat{J}\ell\sum_m \frac{\sin(k_0\ell m)}{m^2}\right]. \qquad (6)$$

The variable v_g is null if $\hat{J} = \hat{J}_{\rm cr}(k_0)$, positive if $\hat{J} < \hat{J}_{\rm cr}(k_0)$, and negative if $\hat{J} > \hat{J}_{\rm cr}(k_0)$. The variable $\hat{J}_{\rm cr}(k_0)$ is the critical value of the dipole-dipole coupling interaction and is given by $\hat{J}_{\rm cr}(k_0) = k_2\sin(k_0\ell)/\sum_m[\sin(k_0\ell m)/m^2]$. The variation of $\hat{J}_{\rm cr}(k_0)$ according to the wave vector k_0 is depicted in Fig. 2. Figure 2 not only confirms the prediction made on Fig. 1(b) (namely that for $k_0\ell < 0.4\pi$ the group velocity is negative, while it is positive for $k_0\ell > 0.4\pi$), but it also shows that it is possible to obtain waves with null group velocity apart from

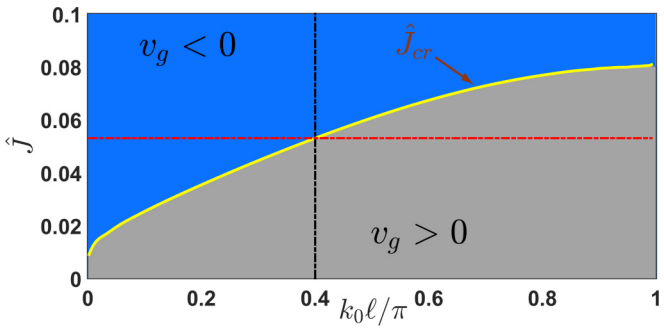

FIG. 2. Critical dipole-dipole coupling constant $\hat{J}_{\rm cr}$ as a function of wave vector k_0. The zone colored in gray (or in blue) in this figure represents the parameter region for a positive (or negative) group velocity.

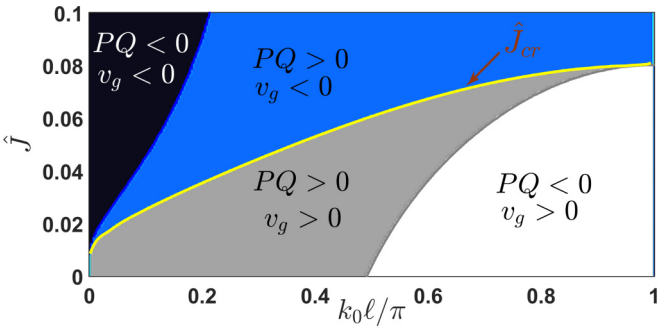

FIG. 3. Chart of the existence of bright and dark solitons as well as the sign of the group velocity as a function of the wave vector and the dipole-dipole coupling constant.

the center ($k_0\ell = 0$) and the upper limit ($k_0\ell = \pi$) of the first Brillouin zone.

B. Nonlinear analysis

Due to the fact that the mathematical model of Eq. (3) is less straightforward to tackle directly, the semidiscrete (or quasicontinuum) approximation is adopted [53,54]. The approach assumes that the solution of Eq. (3) is under the form

$$Y_n(\tau) = \varepsilon F_1(\varepsilon n\ell, \varepsilon\tau)e^{i\theta_n} + \varepsilon^2[F_0(\varepsilon n\ell, \varepsilon\tau) + F_2(\varepsilon n\ell, \varepsilon\tau)e^{2i\theta_n}] + \text{c.c.} + O(\varepsilon^3), \tag{7}$$

where $\theta_n = n\ell k_0 - \omega\tau$, $F_1(\varepsilon n\ell, \varepsilon\tau)$, and $F_2(\varepsilon n\ell, \varepsilon\tau)$ are complex functions and c.c. is their complex conjugate, $i^2 = -1$, $F_0(\varepsilon n\ell, \varepsilon\tau)$ is a real function, ω and k_0 denote the carrier's frequency and wave number, respectively, and ε is a formal small parameter. By inserting Eq. (7) into Eq. (3) and collecting the terms in different orders of ε and $e^{i\theta_n}$, the functions F_0 and F_2 can be expressed as functions of F_1:

$$F_0 = \mu|F_1|^2, \quad F_2 = \delta F_1^2, \quad \mu = \frac{2\alpha\omega_g^2}{\omega_g^2 + 2\hat{J}\sum_m \frac{1}{m^3}},$$
$$\delta = \frac{\alpha\omega_g^2}{\omega_g^2 + 4k_2\sin^2(k_0\ell) - 4\omega^2 + 2\hat{J}\sum_m \frac{\cos(2k_0\ell m)}{m^3}}. \tag{8}$$

By using Eq. (8), one can show that F_1 is a solution of the nonlinear Schrödinger (NLS) equation [31,33]:

$$i\frac{\partial F_1}{\partial\tau} + P\frac{\partial^2 F_1}{\partial\eta^2} + Q|F_1|^2F_1 = 0, \tag{9}$$

where the coefficients of dispersion (P) and nonlinearity (Q) are

$$P = \frac{1}{2\omega}\left[k_2\ell^2\cos(k_0\ell) - v_g^2 - \hat{J}\ell^2\sum_m \frac{\cos(k_0\ell m)}{m}\right], \tag{10}$$

$$Q = \frac{1}{2\omega}\left[-\omega_g^2[3\beta - 2\alpha(\delta+\mu)] + 48k_4\sin^4\left(\frac{k_0\ell}{2}\right)\right], \tag{11}$$

with the group velocity (v_g) given in Eq. (6), and $\eta = \varepsilon(n\ell - v_g\tau)$ is the rescaled space variable. It is well known that the NLS equation possesses soliton solutions whose specific nature is governed by the signs of the coefficients P and Q [53–56]. In particular, if $PQ > 0$, the NLS equation supports bright soliton solutions, while for $PQ < 0$ it supports dark soliton solutions [53–56]. In the case under consideration, the signs of the coefficients P and Q for Eq. (9) depend not only on the frequency ω but also on the dipole-dipole coupling constant $\hat{J}$. The sign of the product PQ as a function of k_0 and $\hat{J}$ is depicted in Fig. 3. It can be noticed that the dipole-dipole coupling constant influences considerably the types of solitons. For the absence or very low values of the LRI ($\hat{J} \leqslant 0.012\,35$), the system supports only forward propagating breathers. For $\hat{J} \in [0.012\,35, 0.081\,33]$, there are possibilities to have both forward and backward waves. When $\hat{J} > 0.081\,33$, only the backward waves (pulse/dark) exist in the system. Therefore, various soliton solutions (pulse or dark) with positive (forward wave) or negative (backward wave) group velocity emerge from specific values of the wave vector and LRI. Thus, the LRI enriches the system dynamics.

Bright breatherlike modes can mimic and match the experimentally observed local fluctuational opening as well as bubbles propagating along the DNA lattice [27,28]. The analysis of the present study is therefore restricted to the particular case $PQ > 0$.

By using the known analytical pulse soliton solution of Eq. (9) [53–56], and the relations given by Eq. (8), the resulting solution from the ansatz Eq. (7) is

$$Y_n(\tau) = 2\varepsilon\sqrt{\frac{2P}{Q}}u_0\,\mathrm{sech}\{\varepsilon u_0[n\ell - (v_g + 2\varepsilon PL_0)\tau]\} \times \left\{\cos\left\{(\varepsilon L_0 + k_0)n\ell - \left[\omega + \varepsilon L_0 v_g + \varepsilon^2 P\left(L_0^2 - u_0^2\right)\right]\tau\right\}\right\}$$
$$+ 2\varepsilon^2\left(\frac{2P}{Q}\right)u_0^2\,\mathrm{sech}^2\{\varepsilon u_0[n\ell - (v_g + 2\varepsilon PL_0)\tau]\} \times \left\{\frac{\mu}{2} + \delta\cos\left\{2(\varepsilon L_0 + k_0)n\ell - 2\left[\omega + \varepsilon L_0 v_g + \varepsilon^2 P\left(L_0^2 - u_0^2\right)\right]\tau\right\}\right\}, \tag{12}$$

with u_0 and L_0 constants of integration.

To validate the previous analytical approximation, the discrete equation (2) is numerically integrated by means of the standard fifth-order Runge-Kutta scheme with periodic boundary conditions, and a time step chosen small enough to conserve the energy of the system. The initial conditions $Y_n(\tau = 0)$ and $\dot{Y}_n(\tau = 0)$ for numerical integration are derived from Eq. (12). The other constants necessary for this simulation are $\varepsilon = 0.1$, $\ell = 1$, $u_0 = 1$, and $L_0 = 0$. The results are displayed in Figs. 4 and 5. In the panels of Fig. 4, $\hat{J} = 0.02$ and $k_0\ell = 0.45\pi$. This value of the wave vector corresponds to the forward bright solution analytically predicted in Fig. 3 (case $PQ > 0$, $v_g > 0$). Panel (a) of Fig. 4 shows the spatiotemporal dynamic of the breather, while panel (b) shows the snapshot evolution of the analytical solution given by Eq. (12) (gray line) as well as the numerical solution (gray circle) at time $\tau = 1000$, which demonstrates a good agreement with our analytical predictions. However, since

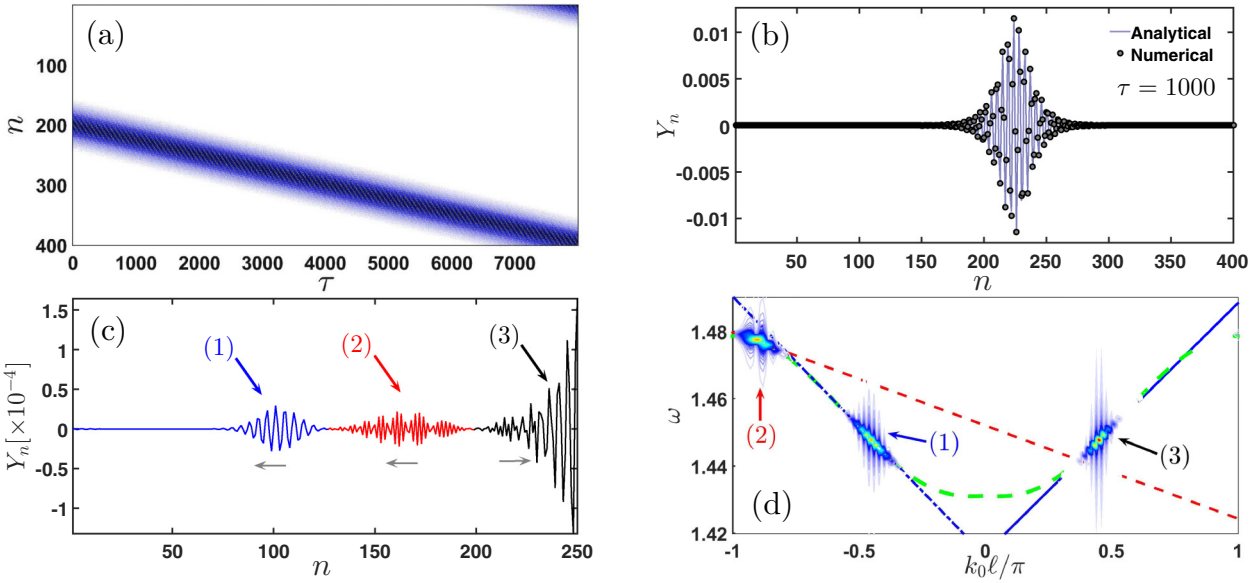

FIG. 4. Spatial and temporal evolution of the breather [panel (a)] and the snapshots of the evolution of the analytical/numerical solution [panel (b)] of the forward wave solution of Eq. (2) for $\hat{J} = 0.02$ and $k_0\ell = 0.45\pi$. Panel (c) represents only the zoom of the numerical solution given out in panel (b) at time $\tau = 4000$ and for $n \in [1, \quad 250]$, where we observe two very-low-amplitude quasilinear wave packets [indexed by (1) and (2)], which move in the opposite direction of the initial excitation indexed by (3). Panel (d) represents the 2D DFT [see Eq. (14)] of the moving breather given in panel (a). The green dashed curve is the linear dispersion curve given by Eq. (5) while the line is for $\omega^{(p)} = \omega_c^{(p)} + \mathcal{V}^{(p)}(k_0 - k_c^{(p)})$ $(p = 1, 2, 3)$ with $k_c^{(1)} = -0.45\pi$, $\omega_c^{(1)} \approx 1.448$, $\mathcal{V}^{(1)} \approx -2.4551 \times 10^{-2}$ (blue dotted line), $k_c^{(2)} = 2k_c^{(1)}$, $\omega_c^{(2)} \approx 1.477$, $\mathcal{V}^{(2)} \approx -8.8176 \times 10^{-3}$ (red dotted line), and $k_c^{(3)} = -k_c^{(1)}$, $\omega_c^{(3)} = \omega_c^{(1)}$, $\mathcal{V}^{(3)} = -\mathcal{V}^{(1)}$ for the blue line. To see clearly the emitted waves (1) and (2) of panel (c) in the 2D DFT, we magnified each of those waves by 500.

the obtained solution given in Eq. (12) is the approximative solution for the real discrete system, the space-time evolution of the breather will generate tails of oscillations or relatively small nonlinear/quasilinear extended waves called wings [57]. A zoom of the solution in Fig. 4(c) illustrates that the propagation of the main nonlinear wave indexed by (3) radiates

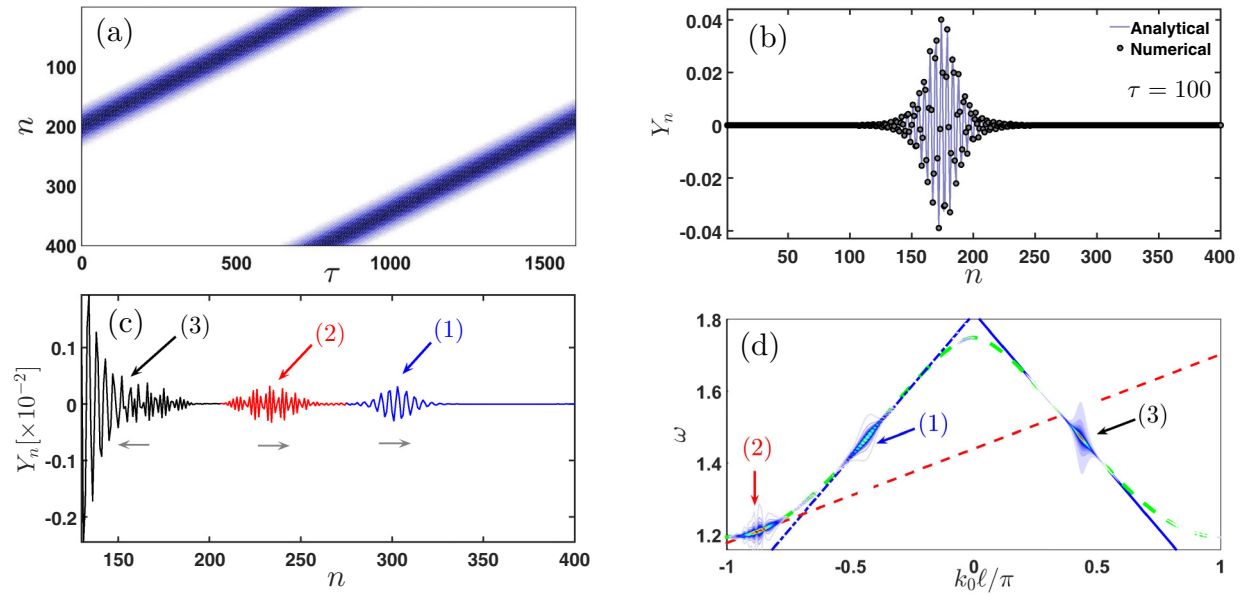

FIG. 5. Spatial and temporal evolution of the breather [panel (a)] and the snapshots of the evolution of the analytical/numerical solution [panel (b)] of the backward wave solution of Eq. (2) for $\hat{J} = 0.442$ and $k_0\ell = 0.4337\pi$. Panel (c) represents only the zoom of the numerical solution given out in panel (b) at time $\tau = 400$ and for $n \in [130, 400]$, where we observe two very-low-amplitude quasilinear wave packets [indexed by (1) and (2)] which move in the opposite direction of the initial excitation indexed by (3). Panel (d) represents the 2D DFT [see Eq. (14)] of the moving breather given in panel (a). The green dashed curve is the linear dispersion curve given by Eq. (5), while the line is for $\omega^{(p)} = \omega_c^{(p)} + \mathcal{V}^{(p)}(k_0 - k_c^{(p)})$ $(p = 1, 2, 3)$ with $k_c^{(1)} = -0.4337\pi$, $\omega_c^{(1)} \approx 1.467$, $\mathcal{V}^{(1)} \approx +0.2562$ (blue dotted line), $k_c^{(2)} = 2k_c^{(1)}$, $\omega_c^{(2)} \approx 1.212$, $\mathcal{V}^{(2)} \approx +8.3632 \times 10^{-2}$ (red dotted line), and $k_c^{(3)} = -k_c^{(1)}$, $\omega_c^{(3)} = \omega_c^{(1)}$, $\mathcal{V}^{(3)} = -\mathcal{V}^{(1)}$ for the blue line. To see clearly the emitted waves (1) and (2) of panel (c) in the 2D DFT, we magnified each of those waves by 75.

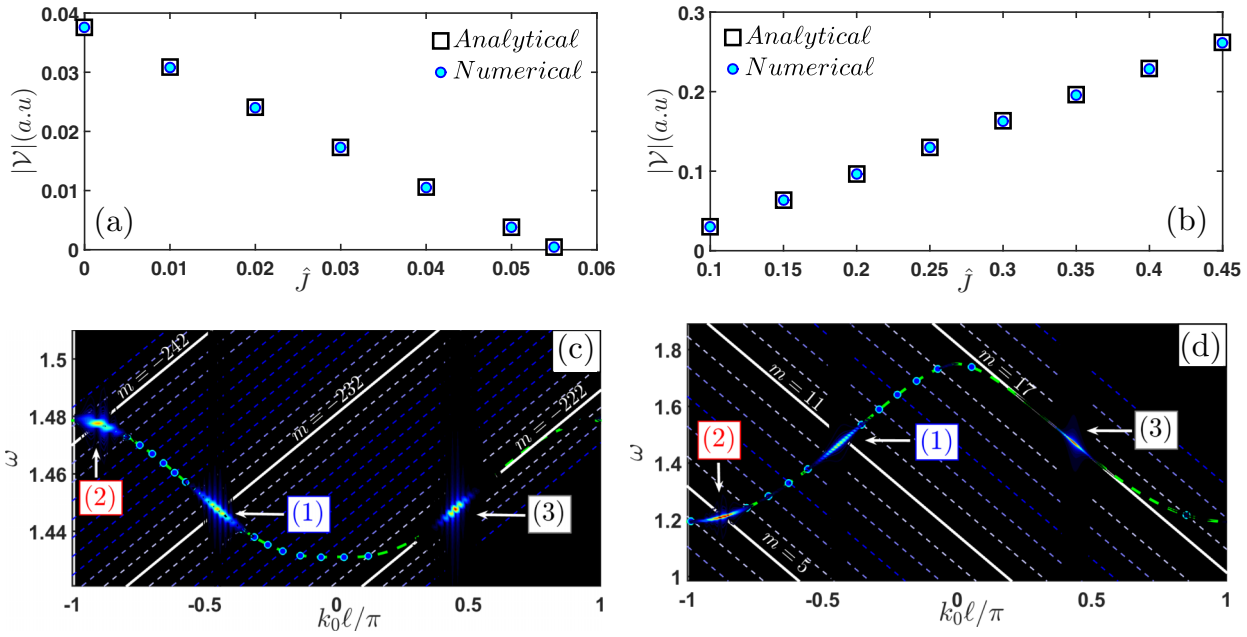

FIG. 6. (a), (b) Variation of the breather velocity as a function of the LRI. The analytical velocity stands for the group velocity v_g [Eq. (6)] while its numerical analog [Eq. (13)] is computed after solving the full discrete system given by Eq. (2). For all these panels, $k_0\ell = 0.4337\pi$. (c), (d) 2D DFT of waves (1), (2), and (3) of Figs. 4(c) and 5(c) as well as the lines and intersection points of breather (3) with phonon mode.

two very-low-amplitude wave packets [indexed by (1) and (2)], which both move in the opposite direction of the initial excitation. To know if waves (1) and (2) of Figs. 4(c) and 5(c) are nonlinear or quasilinear waves, it would be judicious to perform the two-dimensional discrete Fourier transform of the moving breather.

C. Two-dimensional discrete Fourier transform

It is well known that certain information and characteristics of a signal that are hidden in the spatiotemporal domain (n, τ) can be emphasized in the frequency domain (k_0, ω). To explore in-depth the response of the discrete lattice, the two-dimensional discrete Fourier transform (2D DFT) of the solution given by Eq. (12) is used. The traveling breather in the frequency domain *moves* along a line $\omega = \omega_c + \mathcal{V}(k_0 - k_c)$ in (k_0, ω) space, where k_c and ω_c are, respectively, the frequency and wave number of a carrier wave [58]. The variable $\mathcal{V}$ is the velocity (slope) of the moving wave, and it can be numerically estimated through Eqs. (13):

$$\mathcal{V} = \frac{1}{\mathcal{T}} \sum_{k=1}^{\mathcal{T}_k} \dot{\mathcal{Y}}(\tau_k), \quad \mathcal{Y}(\tau_k) = \frac{\sum_{n=1}^{N} n Y_n^2(\tau_k)}{\sum_{n=1}^{N} Y_n^2(\tau_k)}, \tag{13}$$

where $\mathcal{T}$ is the simulation duration, $\mathcal{T}_k$ the number of time steps, and $\mathcal{Y}(\tau_k)$ is the evolution of the pseudocenter of mass of the breather [51].

By using the 2D DFT formula below [58],

$$\tilde{Y}(k_0, \omega) = \sum_{p=0}^{\tau_p=\tau} \sum_{q=0}^{N-1} Y_q(\tau_p) \exp[-i(k_0 \ell x_q - \omega \tau_p)], \tag{14}$$

the moving breather dynamics are represented in Figs. 4(d) and 5(d). The breather amplitude $|\tilde{Y}(k_0, \omega)|$ is displayed by a heat map [low (blue) to red (high) values], and the green dashed curve is the linear dispersion curve given by Eq. (5).

The analysis of Fig. 4(d) shows that the breather velocity ($\mathcal{V}^{(3)} \approx 2.4551 \times 10^{-2}$) is almost equal at the group velocity ($v_g \approx 2.4603 \times 10^{-2}$), and the direction of propagation of the breather is according to the line $\omega^{(3)} = \omega_c^{(3)} + \mathcal{V}^{(3)}(k_0 - k_c^{(3)})$ (given by the solid blue curve) with $\omega_c^{(3)} \approx 1.448$ and $k_c^{(3)} = 0.45\pi$. It is noticed that the velocity of the breather decreases or increases for lower or higher values of the LRI coefficient, respectively [Figs. 6(a) and 6(b)].

The same observation is made in Fig. 5(d), where the breather propagation follows the line $\omega^{(3)} = \omega_c^{(3)} + \mathcal{V}^{(3)}(k_0 - k_c^{(3)})$ with $k_c^{(3)} = 0.4337\pi$, $\omega_c^{(3)} \approx 1.467$, and $\mathcal{V}^{(3)} \approx -0.2562$ while $v_g \approx -0.2565$.

Careful analysis and observation during evolution of wave (1) in Fig. 4(c) reveals that it is a very low nonlinear wave propagating symmetrically but in the opposite direction to the wave (3). Indeed, its 2D DFT shows that it follows the line given by $\omega^{(1)} = \omega_c^{(1)} + \mathcal{V}^{(1)}(k_0 - k_c^{(1)})$ with $\omega_c^{(1)} \approx 1.448$, $k_c^{(1)} = -0.45\pi$, and $\mathcal{V}^{(1)} = -2.4551 \times 10^{-2}$. By carrying out a similar analysis to wave (2), we see that it is a quasilinear wave that propagates along the line $\omega^{(2)} = \omega_c^{(2)} + \mathcal{V}^{(2)}(k_0 - k_c^{(2)})$ with $\omega_c^{(2)} \approx 1.477$, $k_c^{(2)} = 2k_c^{(1)}$, and $\mathcal{V}^{(2)} = -8.8176 \times 10^{-3}$. It should be noted that wave (1) keeps its shape and speed almost constant for a fairly long evolution time, while wave (2) disappears for the same time. The analysis performed for the case of Fig. 4(c) can be transposed to Fig. 5(c) with $\omega_c^{(1)} \approx 1.467$, $k_c^{(1)} - 0.4337\pi$, $\mathcal{V}^{(1)} = +0.2562$, $\omega_c^{(2)} \approx 1.212$, $k_c^{(2)} = 2k_c^{(1)}$, and $\mathcal{V}^{(2)} = +8.3632 \times 10^{-2}$. It should be noted that in order to be able to observe the waves (1) and (2) in the plane (ω, k_0), we have magnified them by 500 (for the case of Fig. 4) and by 75 (for the case of Fig. 5).

D. Resonant breather with the phonon band

The moving approximated solution given by Eq. (12) repeats itself after a time $\tau' = \tau + qT_b$, but it shifts from its initial position ($n' \to n \pm p$), with p, q integers and $T_b = 2\pi/\omega_b$ the breather period. This approximate solution could be resonant with the phonon mode. These resonant (p/q) moving breathers would then obey the following relation:

$$Y_{n\pm p}(\tau + qT_b) = Y_n(\tau), \ \forall\, n. \tag{15}$$

Given that this breather would resonate with the plane wave of phonon modes, we could then apply *the plane-wave ansatz* (see Sec. II A) to Eq. (15), which leads to the condition [67]

$$\frac{\omega}{\omega_b} = \frac{1}{q}\left[\pm\left(\frac{k_0\ell}{2\pi}\right)p - m\right], \tag{16}$$

with ω_b the breather frequency, m being any integer, and ω is given in Eq. (5). By using the values of the pair (k_0, ω) corresponding to the line of breather propagation on the one hand and the Gauss-Newton method on the other hand, it is possible to obtain the integers p, q, and m associated with the corresponding moving breather. Once p, q, and m have been obtained, it then becomes possible to calculate in a more general way all the values of m by combining Eqs. (16) and (5) through

$$m = \pm\left(\frac{k_0\ell}{2\pi}\right)p \mp \frac{q}{\omega_b} \times \sqrt{\omega_g^2 + 4k_2\sin^2\left(\frac{k_0\ell}{2}\right) + 2\hat{J}\sum_s \frac{\cos(k_0\ell s)}{s^3}}, \tag{17}$$

as well as the intersection points with the phonon band (k_{0j}, ω_j).

Figures 6(c) and 6(d) give the 2D DFT of the solutions shown in Figs. 4(a) and 5(a), respectively. We can see in these figures that the small wave amplitudes (1) and (2) highlighted in Figs. 4(c) and 5(c) originate from the resonance of breather (3) with the phonon mode as evidenced by the oblique white line. The dashed lines (which are the intersection lines) as well as the blue filled circles (which are the intersection points) come from Eqs. (17) and (16).

The diagram displayed in Fig. 3 shows that for $\hat{J} \in [0.012\,35, 0.081\,33]$, it is possible to have a coexistence of bright breathers having positive, negative, or null group speeds depending on the wave vector k_0. Consequently, one can expect to have an interaction (collision) between the forward, backward, and stationary waves. To verify this, Eq. (2) is simulated with superpositions of initial conditions derived from Eq. (12), and corresponding to the forward, backward, or stationary propagating breather solution. The results of these simulations are displayed in Fig. 7, showing four types of collision: the forward-forward collision [Fig. 7(a)], the backward-backward collision [Fig. 7(b)], the forward-backward collision [Fig. 7(c)], and the forward-stationary-backward collision [Fig. 7(d)]. Figure 7 confirms the prediction made in Fig. 3 and shows that after the interaction (collision) of the various solutions, emergent breathers maintain their shapes and speeds (a key characteristic of a soliton [54]).

III. IDENTIFYING STATIONARY DISCRETE BREATHERS

The NLS-model reduction is used to identify an initial ansatz of an approximate soliton solution, subsequently introduced in the original dynamical lattice to assess its potential robustness. In contrast to previous studies of breathers in DNA [27,28,31–33], here we do not restrict our considerations to that. We went a step further toward a numerical calculation of the "*true*" nonlinear bright breather solutions (up to a prescribed numerical accuracy) and assessing their spectral stability.

It was demonstrated that breathers of small amplitude that are highly localized describe the information transfer in DNA [27,28]. Thus, the low amplitude breather solution estimated in the previous section through a perturbation approach can be a good initial profile in our quest for the exact DB. Our attention here will be focused on the discrete bright breatherlike solutions, which means that the following conditions must be satisfied:

$$Y_n(\tau) = Y_n\left(\tau + \frac{2\pi}{\omega_b}\right), \quad \lim_{|n|\to\infty} Y_n = 0. \tag{18}$$

Here, ω_b and $T_b = 2\pi/\omega_b$ are the DB frequencies and periods, respectively. It should be noted that these solutions exist if and only if the condition of nonresonance with the phonon modes is fulfilled, namely $z \times \omega_b \neq \omega(\hat{J}, k_0)$, where $\omega(\hat{J}, k_0)$ is the linear spectrum frequency of the system given by Eq. (5), and z is an integer [1–4]. Various methods can be used to find the DB solutions to Eq. (2). In this study, the iterative Newton-Raphson method, which makes possible the obtention of the discrete breatherlike solutions with a relatively high accuracy, is employed [59]. The true challenge of the Newton-Raphson method resides in the suitable choice of the initial condition. Indeed, it is well known that when this initial condition is not close to the sought solution, the method does not converge [59]. Since we are interested in discrete bright breathers, we will use the procedure of Refs. [38–40]. For this purpose, the NLS bright soliton solution estimated in Eq. (12) is used as the initial condition for the Newton-Raphson method to estimate numerically the exact periodic motion.

As the initial solution is static, a standing-wave profile ($v_g = 0$) can be determined with values of the wave number k_0 and $\hat{J}$ suitably chosen [solving the equation $v_g = 0$ based on Eq. (6)]. In addition, since the solution with the typical exponential decay amplitude is supported in the k_0-parameter range where the product PQ of the NLS equation (9) demonstrates focusing behavior (i.e., $PQ > 0$), Figs. 2 and 3 show the appropriate choices of this wave number, which are $k_0\ell = 0$ for $\hat{J} \in [0, 0.01235]$, $k_0\ell = \pi$ for $\hat{J} \in [0.08133, 0.37]$, and for $\hat{J} \in\,]0.012\,35, 0.081\,33[$ for values of $k_0\ell$ pertaining to $\hat{J}_{\rm cr}$. The long-range coefficient modifies the allowed bandwidth $\Delta\omega = \omega_{\rm max} - \omega_{\rm min}$ of the phonon modes [see Fig. 1(d)]. Thus it appears that values of $\hat{J}$ should be carefully selected.

To fulfill the nonresonance condition, a value of the breather frequency ω_b is suitably chosen such that the second harmonic $2\omega_b$ of this frequency lies above the value of $\omega_{\rm max}(\hat{J}, k_0)$.

Once the periodic and localized solution $\hat{Y}_n(\tau)$ [condition Eq. (18)] is obtained, it is important to study its stability. For

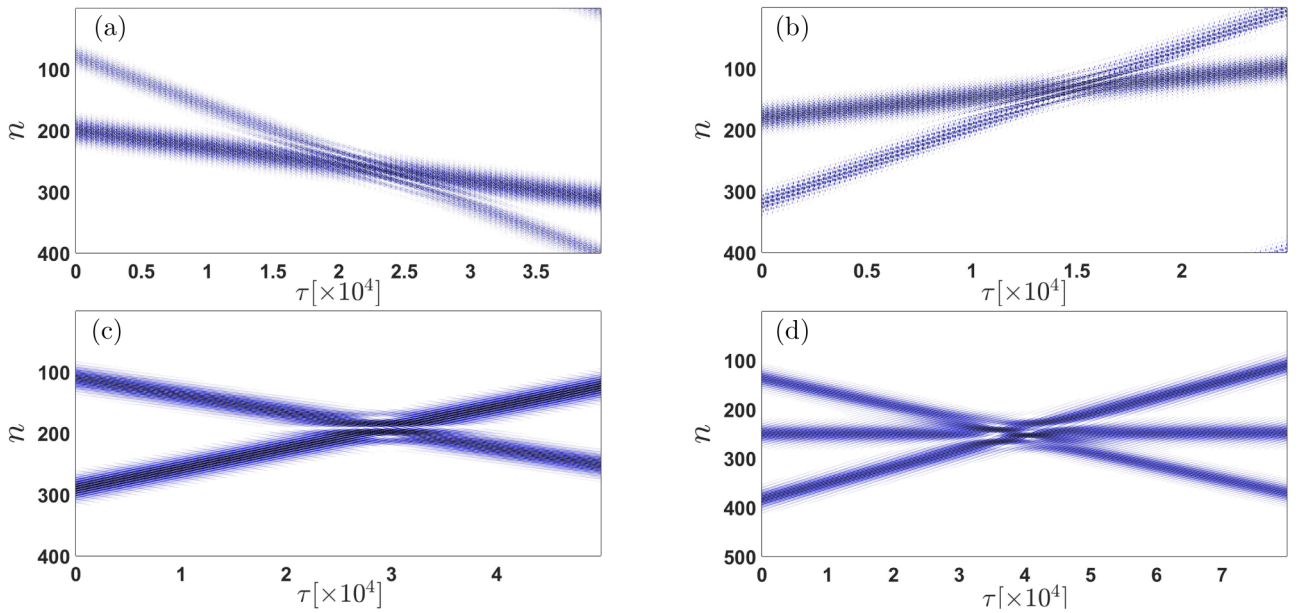

FIG. 7. Contour plot showing four types of spatiotemporal collision of forward and backward waves: (a) Forward-forward collision obtained for $k_1^0\ell = 0.620\pi$ ($v_{g1} = 8.072 \times 10^{-3}$, $A_{\max 1} = 8.327 \times 10^{-3}$) and $k_2^0\ell = 0.454\pi$ ($v_{g2} = 2.820 \times 10^{-3}$, $A_{\max 2} = 1.602 \times 10^{-2}$); (b) backward-backward collision obtained for $k_1^0\ell = 0.344\pi$ ($v_{g1} = -3.268 \times 10^{-3}$, $A_{\max 1} = 1.788 \times 10^{-2}$) and $k_2^0\ell = 0.152\pi$ ($v_{g2} = -1.277 \times 10^{-2}$, $A_{\max 2} = 1.035 \times 10^{-2}$); (c) forward-backward collision obtained for $k_1^0\ell = 0.454\pi$ ($v_{g1} = 2.820 \times 10^{-3}$, $A_{\max 1} = 1.602 \times 10^{-2}$) and $k_2^0\ell = 0.344\pi$ ($v_{g2} = -3.268 \times 10^{-3}, A_{\max 2} = 1.788 \times 10^{-2}$); (d) forward-stationary-backward collision obtained for $k_1^0\ell = 0.454\pi$ ($v_{g1} = 2.820 \times 10^{-3}$, $A_{\max 1} = 1.602 \times 10^{-2}$), $k_2^0\ell = 0.400\pi$ ($v_{g2} = 0$, $A_{\max 2} = 1.721 \times 10^{-2}$), and $k_3^0\ell = 0.344\pi$ ($v_{g3} = -3.268 \times 10^{-3}$, $A_{\max 3} = 1.788 \times 10^{-2}$). For all these simulations, the value of the dipole-dipole coupling constant is fixed at $\hat{J} = 0.053$. [Note: $A_{\max}$ and v_g stand for maximum amplitude and group velocity of the breather, respectively. The index $1, 2, \ldots$ stands for each individual breather during initial superposition. The numerical simulation results [Eq. (2)] and the analytical solution [Eq. (12)] agree. For the sake of clarity, they are not compared as in Figs. 4(b) and 5(b) to avoid an overload of the plotted graphs.]

that purpose, an infinitesimal perturbation $\chi_n(\tau)$ is added to it [$Y_n(\tau) = \hat{Y}_n(\tau) + \chi_n(\tau)$] and the equation of motion (2) is linearized with respect to $\chi_n(\tau)$:

$$\begin{aligned}
&\ddot{\chi}_n + \frac{2K_b}{a^2 D}(2\chi_n - \chi_{n+1} - \chi_{n-1}) + \sum_{i\neq n} \hat{J}_i \chi_{n+i} \\
&+ \frac{2b\Delta H}{a^2 DC}\left[1 - \frac{2b}{a^2}\left(\hat{Y}_n - \hat{Y}_{n-1}\right)^2\right](\chi_n - \chi_{n-1}) \\
&\times e^{-\frac{b}{a^2}\left(\hat{Y}_n - \hat{Y}_{n-1}\right)^2} - \frac{2b\Delta H}{a^2 DC}\left[1 - \frac{2b}{a^2}\left(\hat{Y}_{n+1} - \hat{Y}_n\right)^2\right] \\
&\times (\chi_{n+1} - \chi_n) e^{-\frac{b}{a^2}\left(\hat{Y}_{n+1} - \hat{Y}_n\right)^2} \\
&+ 2\left(2e^{-\hat{Y}_n} - 1\right)e^{-\hat{Y}_n}\chi_n = 0. \qquad (19)
\end{aligned}$$

To identify the orbital stability of these solutions, Floquet's analysis can be performed. Floquet's method is commonly accepted for the DB stability analysis [2,5]. A solution $\hat{Y}_n(\tau)$ is considered stable when, for any initial conditions, the linear perturbation $\chi_n(\tau)$ does not grow exponentially with time. When $\hat{Y}_n(\tau)$ is time-periodic with period T_b, then Eq. (19) defines a linear map between the initial perturbation at $\tau = 0$ and the perturbation at time $\tau = T_b$, expressed by a matrix $\mathcal{M} = \mathcal{M}(\hat{Y}_n)$, known as the monodromy matrix:

$$\begin{bmatrix} \chi_n \\ \dot{\chi}_n \end{bmatrix}_{\tau = T_b} = \mathcal{M} \times \begin{bmatrix} \chi_n \\ \dot{\chi}_n \end{bmatrix}_{\tau = 0}. \qquad (20)$$

The complex eigenvalues λ and eigenvectors of the $2N \times 2N$ monodromy matrix $\mathcal{M}$ provide information about the stability of the DB. If all eigenvalues modulus $|\lambda|$ are less than (or equal to) 1, then the DB is linearly (or marginally) stable. Otherwise, perturbation effects persist and grow with time (typically exponentially), leading to a linearly unstable DB.

Parameters used for this numerical simulation whose periodic boundary conditions were used are $N = 50$ and $\varepsilon = 0.8$; other parameters such as u_0 and ℓ are unchanged. Figure 8 gives the representation of the solutions obtained by using Eq. (12) as the initial condition. The parameters used to obtain Figs. 8(a) and 8(b) are $k_0\ell = 0$ [(a) $\omega_b = 1.40$, $\hat{J} = 0.0$; (b) $\omega_b = 1.407\,63$, $\hat{J} = 0.011\,115$]; Figs. 8(c) and 8(d) are obtained for $k_0\ell = \pi$ [(c) $\omega_b = 1.417$, $\hat{J} = 0.1$; (d) $\omega_b = 1.35$, $\hat{J} = 0.2$]; while Fig. 8(e) is obtained for $k_0\ell = 0.0275\pi$, $\omega_b = 1.426$, $\hat{J} = 0.0161$, and Fig. 8(f) for $k_0\ell = 0.474\pi$, $\omega_b = 1.4474$, $\hat{J} = 0.058\,74$. After conducting a Floquet stability analysis of the obtained solution, the eigenvalues of the monodromy matrix are projected on the unit circle (see the inset curves). It appears that both cases $k_0\ell = 0$ (with $\omega_b = 1.40$, $\hat{J} = 0.0$ or with $\omega_b = 1.407\,63$, $\hat{J} = 0.011\,115$) and $k_0\ell = \pi$ (with $\omega_b = 1.417$, $\hat{J} = 0.1$ or with $\omega_b = 1.35$, $\hat{J} = 0.2$) give solutions that are linearly stable [see Figs. 8(a)–8(d)]. However, when $\hat{J} = \hat{J}_{\rm cr}(k_0)$, it is observed that for $\hat{J}_{\rm cr} = 0.0161$, the periodic solution of frequency $\omega_b = 1.426$ is linearly stable [see Fig. 8(e)] while the one obtained for $\omega_b = 1.4471$ and $\hat{J}_{\rm cr} = 0.058\,74$ is linearly unstable [see Fig. 8(f)].

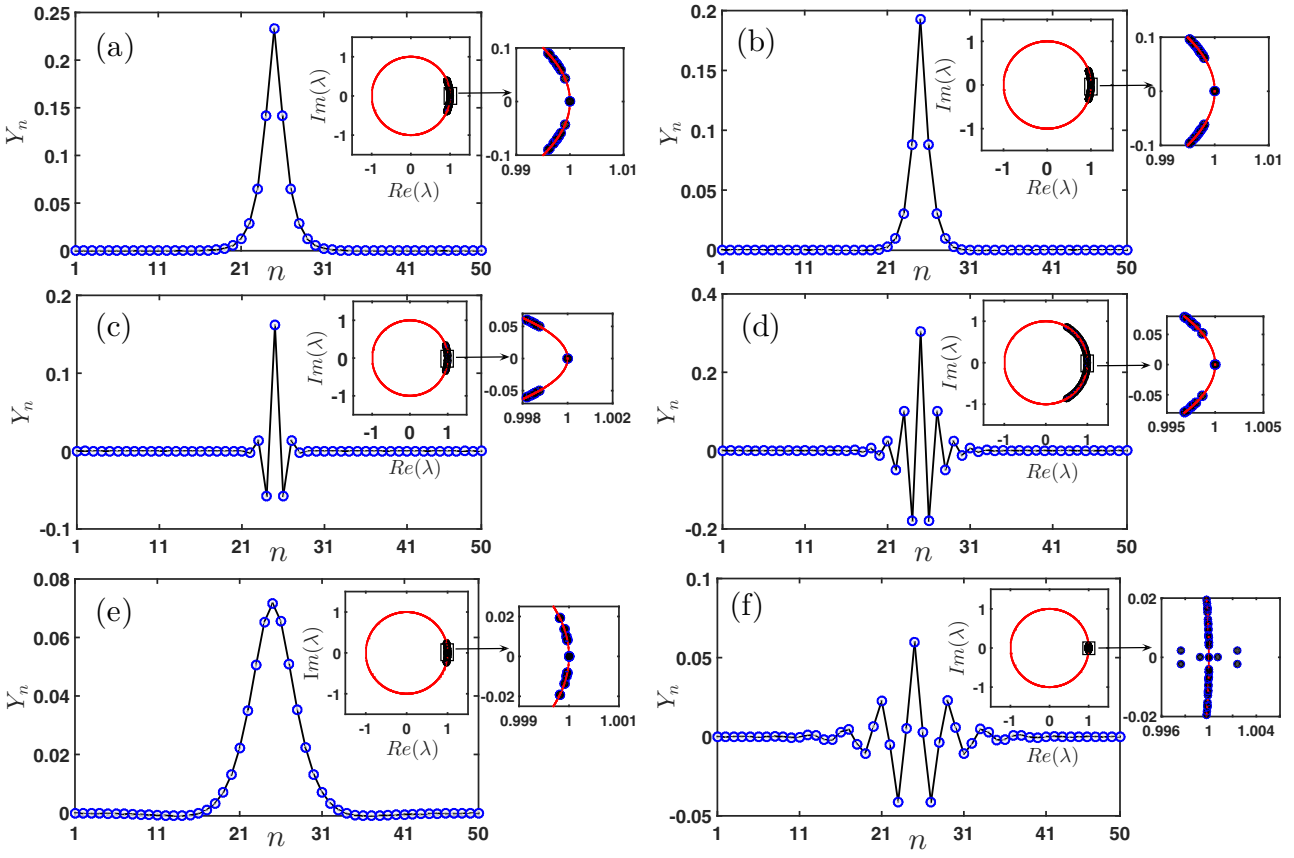

FIG. 8. Family of corrected DBs together with the corresponding Floquet multipliers (inset curve) projected on a unit circle, obtained for $k_0\ell = 0$ [(a) $\omega_b = 1.40$, $\hat{J} = 0.0$; (b) $\omega_b = 1.407\,63$, $\hat{J} = 0.011\,115$], for $k_0\ell = \pi$ [(c) $\omega_b = 1.417$, $\hat{J} = 0.1$; (d) $\omega_b = 1.35$, $\hat{J} = 0.2$], for $k_0\ell = 0.0275\pi$ [(e) $\omega_b = 1.426$, $\hat{J}_{\rm cr} = 0.0161$], and for $k_0\ell = 0.474\pi$ [(f) $\omega_b = 1.4474$, $\hat{J}_{\rm cr} = 0.058\,74$].

Figure 9 displays the energy propagation resulting from the numerical simulation over 8000 periods of the built DBs, as well as the representation of solution Y_n in the (k_0, ω) Fourier space. Figure 9(b) confirms the instability of the solution evidenced by Fig. 8(f). After time $\tau \approx 4000T_b$, the wave is progressively delocalized along the lattice in a noncoherent manner due to interaction with the lattice phonon mode as the 2D DFT shows it (see the inset curve). Moreover, Fig. 9(a) shows that the wave keeps its shape and its localization throughout simulation and does not interact with the phonon mode, thus confirming the stability of the solution obtained in Fig. 8(e). It should be noted that the solutions obtained with Figs. 8(a)–8(d) behave with dynamics nearly similar to that reported in Fig. 8(e).

The 2D DFT of the built stationary solutions shows a clear separation between the position of the discrete breather and the value of the dispersion relation at the considered wave vector k_c. This separation is indeed due to the constructed solution with frequency inside the lower forbidden band gap, and it is still observed in the stationary mode ($\mathcal{V} = 0$), in which the position of the discrete breather is parallel to the line $\omega = \omega_b$ and centered at k_c (see the inset curve of Fig. 9).

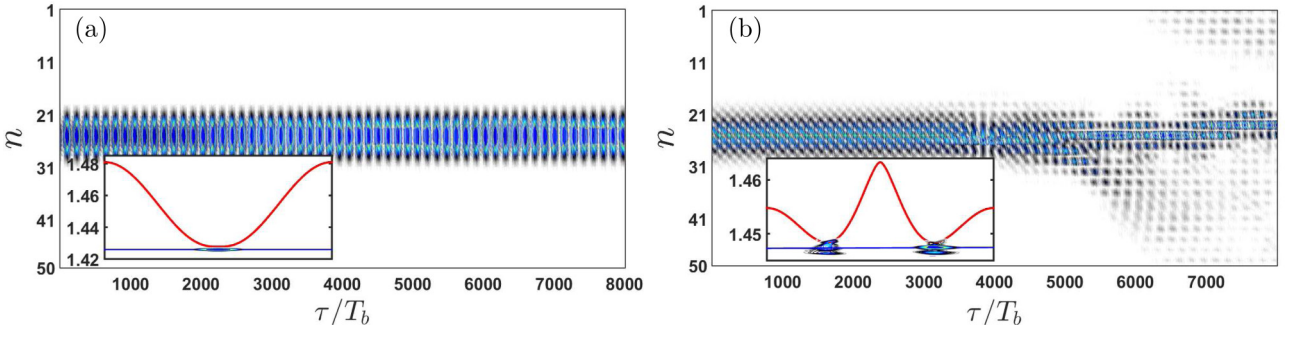

FIG. 9. Contour plot showing spatiotemporal energy propagation of a stable [panel (a): $\omega_b = 1.426$, $\hat{J}_{\rm cr} = 0.0161$, $k_0\ell = 0.0275\pi$] and an unstable [panel (b): $\omega_b = 1.4474$, $\hat{J}_{\rm cr} = 0.05874$, $k_0\ell = 0.474\pi$] discrete breather given by Figs. 8(e) and 8(f), respectively. The inset is the 2D DFT of a stationary DB computed from Eq. (14).

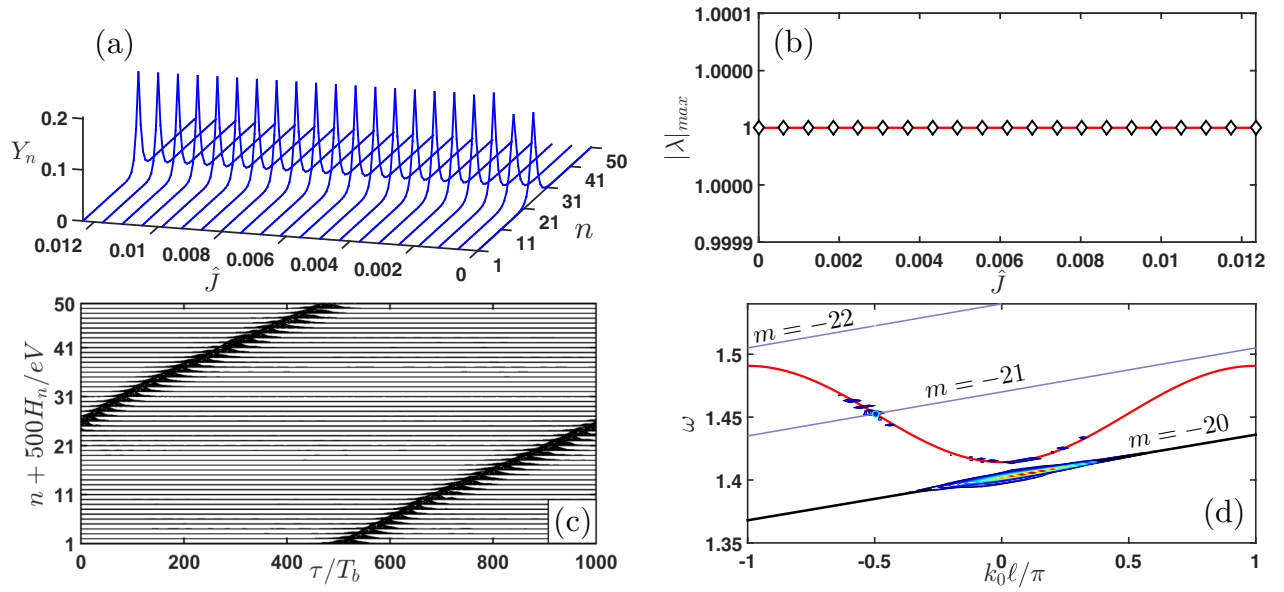

FIG. 10. Profile of corrected discrete breather (a) vs the long-range coefficient parameter $\hat{J}$ obtained for $k_0\ell = 0$. (b) Evolution with respect to dipole-dipole coupling constant $\hat{J}$ of the maximum modulus of the Floquet multiplier. (c) Energy propagation of a MDB emitted by a perturbed SDB for $k_0\ell = 0$, $\hat{J} = 0$, $\omega_b = 1.40$, and $\nu = 0.56$. (d) 2D DFT $|\tilde{Y}(k_0, \omega)|$ in the (k_0, ω) space [given by Eq. (14)] of displacements $Y_n(\tau)$ of the obtained moving discrete breather, where the red curve is the linear dispersion curve given by Eq. (5). The black curve corresponds to the line $\omega = \omega_b + \mathcal{V}(k_0 - k_c)$, with $\omega_b = 1.40$, $k_c = 0$, and $\mathcal{V} \approx 1.084 \times 10^{-2}$, while the gray curves are those obtained by means of Eqs. (16) and (17). The blue filled circle represents the intersection of the resonant breather line with the phonon band.

Once the stationary periodic solution is obtained, the next step is to perform its mobility. Indeed, to be able to answer the proteinic request of the living organism, the DNA molecule needs to be transcribed, which is modeled by a bubble of translation being propagated on the segment of selected DNA for this purpose. The mobility of the exact discrete breather is achieved with the method of Alvarez *et al.* [60], which consists in "kicking" the exact stationary DB solution obtained with the formula

$$\begin{aligned} Y^0_{\mathrm{MDB},n} &= Y^0_{\mathrm{SDB},n} \cos[\nu(n - n_0)], \\ \dot{Y}^0_{\mathrm{MDB},n} &= \pm Y^0_{\mathrm{SDB},n} \sin[\nu(n - n_0)], \end{aligned} \tag{21}$$

where MDB/SDB stand for moving/static discrete breather. The parameter ν refers to a wave number. The $\pm$ sign corresponds to a breather moving forward $(+)$ and backward $(-)$. Note that during their propagation, DBs can interact with the phonon mode. Certainly, achieving mobility of ILM by the "kick" method produces a lot of phonons, but despite this, it is also possible to find the intersection points of the propagating breather with the dispersion curve as performed in Sec. II D.

Due to the fact that $k_0\ell$ is chosen at the middle of the first Brillouin zone ($k_0\ell = 0$), Fig. 10 shows the emergence of a DB solution with neighboring base pairs oscillating spatially in phase, as shown in Fig. 10(a). It can be noticed that for values of $\hat{J} \in]0, 0.012\,35]$, the amplitude of the obtained periodic solutions is a decreasing function of the coefficient $\hat{J}$, while the spatial expansion of the solution grows with LRI. This family of solutions is linearly stable [Fig. 10(b)], and their frequencies vary not linearly according to the law $\omega_b^{\mathrm{app}} = A\hat{J}^r$, with $A = 1.418\,556\,3$ and $r = 0.001\,963\,517\,2$. Using Eq. (21), Fig. 10(c) gives the energy propagation [Eq. (1)] of the obtained MDB for $\hat{J} = 0$, $\omega_b = 1.40$, and $\nu = 0.56$. This energy propagates while passing from site n to site $n + 1$ at each q-period ($q = 20$) and resonates with the phonon band at the point indicated by the blue filled circle [see Fig. 10(d)]. As one can see, this MDB emits phonons that propagate in the opposite direction (negative intersection wave vector), as shown in Fig. 10(d), where we plot the 2D DFT in the (k_0, ω) plane and through which one can see several frequencies interacting with the phonon-dispersion relation.

The analysis of Fig. 10 can be applied to Fig. 11 concerning the amplitude as well as the width of the built periodic solutions. It should be noted, however, that these solutions are obtained for $\hat{J} = \hat{J}_{\mathrm{cr}}(k_0)$. It can be seen in Fig. 11(a) that for certain values of the couples $[k_0, \hat{J}_{\mathrm{cr}}(k_0)]$, the obtained periodic solutions have neighboring base pairs oscillating spatially either in phase or in opposition of phase. These solutions are stable for any $\hat{J}_{\mathrm{cr}}(k_0) \leqslant \hat{J}_{\mathrm{cr}_1}$ (with $\hat{J}_{\mathrm{cr}_1} = 0.023\,212$) while they become unstable for any $\hat{J}_{\mathrm{cr}}(k_0) > \hat{J}_{\mathrm{cr}_1}$ [see Fig. 11(b)] and their frequencies vary also not linearly according to the law $\omega_b^{\mathrm{app}} = A\hat{J}^r_{\mathrm{cr}}(k_0)$ with $A = 1.497\,574\,3$ and $r = 0.007\,233\,644$. The analysis of Figs. 10(c) and 10(d) can still hold for Figs. 11(c) and 11(d) but with $k_0\ell = 0.474\pi$, $\hat{J}_{\mathrm{cr}}(k_0) = 0.058\,74$, $\omega_b = 1.4474$, and $\nu = 0.144\,74$. However, unlike the case of Fig. 10(d), this MDB passes from site n to site $n + 1$ at every $q = 208$ periods and resonates highly with the phonon band, as can be seen in Fig. 11(d), where the blue filled circles represent the intersection points of the resonant DB with the phonon band.

The solutions obtained and reported in Fig. 12 are those corresponding to values of the wave vector chosen at the edge of the first Brillouin zone ($k_0\ell = \pi$). Figure 12(a) shows the emergence of a solution with neighboring base pairs oscillating spatially in opposition of phase, in contrast with the solution at the center of the first Brillouin zone [see

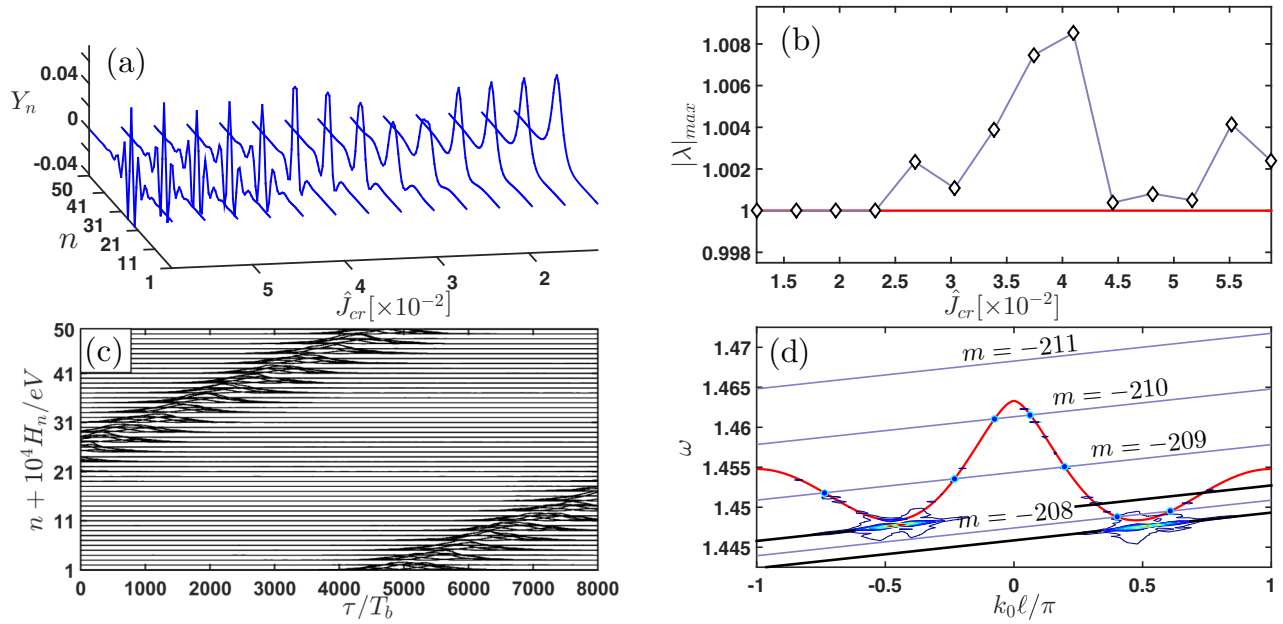

FIG. 11. Profile of corrected discrete breather (a) vs the long-range coefficient parameter $\hat{J}$ obtained for $\hat{J} = \hat{J}_{\rm cr}(k_0)$. (b) Evolution with respect to dipole-dipole coupling constant $\hat{J}$ of the maximum modulus of Floquet's multiplier. (c) The dependence of the DB frequency with respect to $\hat{J}$. Energy propagation of a MDB emitted by a perturbed SDB for $k_0\ell = 0.474\pi$, $\hat{J}_{\rm cr}(k_0) = 0.058\,74$, $\omega_b = 1.4474$, and $\nu = 0.14474$. (d) 2D DFT $|\tilde{Y}(k_0, \omega)|$ in the (k_0, ω) space [given by Eq. (14)] of displacements $Y_n(\tau)$ of the obtained moving discrete breather, where the red curve is the linear dispersion curve given by Eq. (5). The black curves correspond to the lines $\omega = \omega_b + \mathcal{V}(k_0 - k_c)$, with $\omega_b = 1.4474$, $k_c^{\pm} = \pm 0.474\pi$, $\mathcal{V} \approx 1.105 \times 10^{-3}$, while the gray curves are those obtained by means of Eqs. (16) and (17). The blue filled circles represent the intersection points of the resonant breather line with the phonon band.

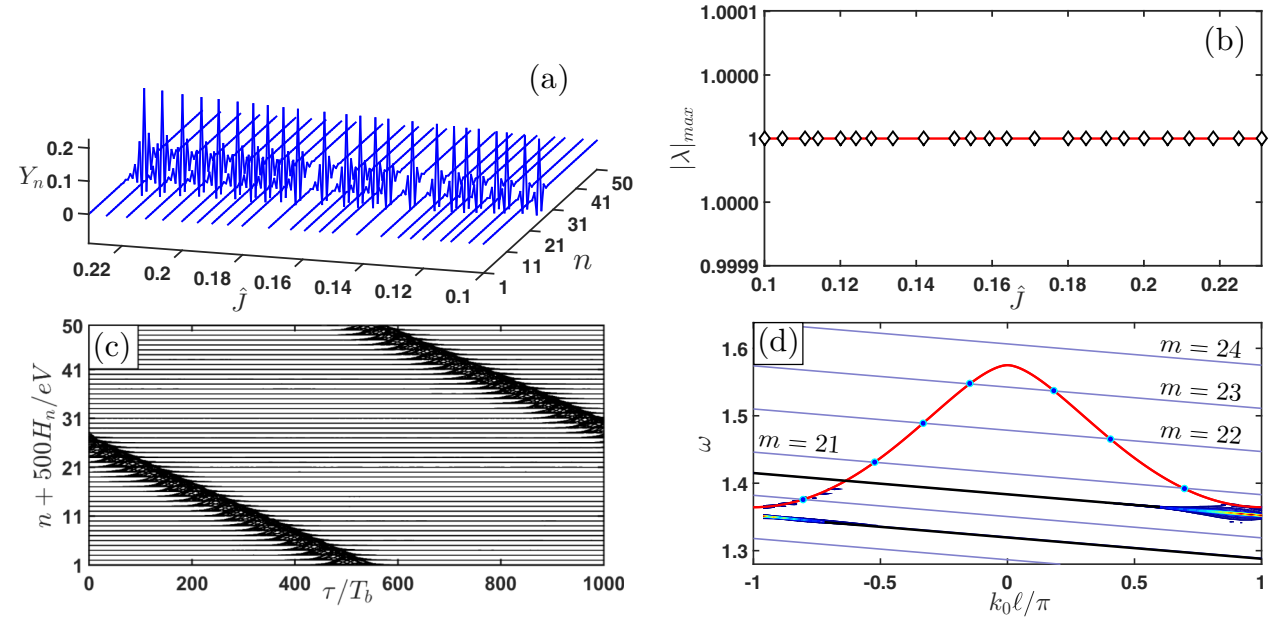

FIG. 12. Profile of corrected discrete breather (a) vs the long-range coefficient parameter $\hat{J}$ obtained for $k_0\ell = \pi$. (b) Evolution with respect to dipole-dipole coupling constant $\hat{J}$ of the maximum modulus of the Floquet multiplier. (c) The dependence of the DB frequency with respect to $\hat{J}$. Energy propagation of a MDB emitted by a perturbed SDB for $k_0\ell = \pi$, $\hat{J} = 0.2$, $\omega_b = 1.35$, and $\nu = 0.27$. (d) 2D DFT $|\tilde{Y}(k_0, \omega)|$ in the (k_0, ω) space [given by Eq. (14)] of displacements $Y_n(\tau)$ of the obtained moving discrete breather where the red curve is the linear dispersion curve given by Eq. (5). The black curves correspond to the lines $\omega = \omega_b + \mathcal{V}(k_0 - k_c)$, with $\omega_b = 1.35$, $k_c = \pi$, $\mathcal{V} \approx -1.01 \times 10^{-2}$ while the gray curves are those obtained by means of the Eqs. (16) and (17). The blue filled circles represent the intersection points of the resonant breather line with the phonon band.

Fig. 10(a)]. These solutions with the wave number closer to the upper cutoff of the first Brillouin zone are linearly stable [see Fig. 12(b)]. Their frequencies vary also not linearly according to the law $\omega_b^{\text{app}} = A\hat{J}^r$, with $A = 1.160\,365\,2$ and $r = -0.090\,687\,018$. The analysis of Figs. 10(c) and 10(d) can apply to Figs. 12(c) and 12(d) but with $k_0\ell = \pi$, $\hat{J} = 0.2$, $\omega_b = 1.35$, and $\nu = 0.27$. Just like the case of Figs. 10(d) and 11(d), this backward MDB propagates from site n to site $n-1$ every 20 periods and also interacts with the phonon band at several points (see the blue filled circles), as shown in Fig. 12(d).

We can observe in Figs. 10(d), 11(d), and 12(d) that the direction of propagation of the moving discrete breather is according to the line $\omega = \omega_b + \mathcal{V}(k_0 - k_c)$, as shown by the black curves in these figures.

IV. DISCUSSION

The analysis of the linear dispersion relation is crucial as the DB mainly vibrates in the forbidden band gap for the avoidance of possible resonances with phonons of the lattice with frequencies inside the allowed frequency band [1–4]. The obtained results show that such analysis is also capital for understanding the nonlinear wave propagation. When the product between the group velocity (v_g) and the phase velocity ($v_{\text{ph}} = \omega/k_0$) is positive, then the soliton moves forward. When this product is negative, there is a backward wave propagation. The latter is frequently encountered in left-handed metamaterials (e.g., [38,43–45]). Surprisingly, it can be seen that the dispersion relation of the DNA, or any other nonlinear lattice models with LRI, did not receive enough attention from this angle [10–14,17–25,41,42]. Different values of $\hat{J}$ change the direction of the wave, and then induce the chameleon behavior emphasized by Togueu *et al.* [46]. More interestingly, stationary bright breathers beyond the edge/center of the first Brillouin zone (wave number different from 0 or π) are obtained solely due to a specific LRI. To our knowledge this has yet to be reported in the literature [10–14,17–25,41,42].

It was demonstrated that bright and dark solitons can be achieved in the same medium, structure and wavelength depending on a slight change of the input condition in an optical waveguide array [61]. A possible alternation of envelope and dark-soliton solutions that depends on the long-range interactions was noticed a long time ago in monatomic/diatomic systems (e.g., Tchawoua *et al.* [47], Remoissenet *et al.* [48], and references therein). Likewise, it is notably observed that semidiscrete dark and bright breathers from the NLS reduction can be supported by the DNA discrete system. Notably, the existence and the modification of the direction of propagation of these two families of solutions are possible in the present model depending solely on the LRI magnitude. The obtained results in the present study, therefore, led us to conclude that a slight change in the LRI can foster the occurrence of dark or bright breathers in a physical system. Note that the semidiscrete dark solution and simulation was purposely not mentioned in this study, which focused solely on the bright breather, which is qualitatively and biologically more relevant for the studied system.

The study of LRI in nonlinear discrete systems has recently attracted more scientific interest. Among the reported phenomena, the LRI modifies the speed and amplitude of the propagating semidiscrete breathers [10], or it induces nonlinear supratransmission [11] and creates on-site DBs [12]. In opposition to the well-known forward waves (FWs) ubiquitously found in various physical media [62,63], the backward waves (BWs) are waves with antiparallel phase and group velocities. The BWs are not mathematical artifacts. They have been highlighted for instance in dusty plasma crystals [64,65]. In electrodynamics, they correspond to the opposition between field momentum connected to the phase velocity and the Poynting vector, which is connected to the group velocity [66]. Depending on the system parameters of physical devices such as a nonlinear discrete transmission electrical line, the microwave moving breather can have its wavelets and wave packets traveling in opposite directions, thus exhibiting either BW or FW behavior [45,46]. The present study shows the possibility of CB in the model as noticed in the short-range-interacting nonlinear discrete electrical transmission line [46].

In the literature, it is demonstrated that quasidiscrete backward and forward waves can interact [51,52], or they can be generated separately depending on the system parameter [46]. It is demonstrated here that their discrete analog can also be generated depending on the specific carrier wave number and LRI intensity. Moreover, it can be noticed that the obtained mobile discrete breather from the perturbation procedures is not an exact solution of the dynamical equations because they have peaks inside the phonon band, and they are naturally expected to radiate small-amplitude waves. They have a finite life because they radiate phonons. This fact occurs because a mobile discrete breather has two frequencies: one due to the internal vibration and another one due to the periodic translation, which is smaller than the first one and is responsible for the resonance with the phonons, and thus of their emission [2,3]. The precise numerical computation of traveling bright breathers using Newton-Raphson-type methods and their stability analysis through Floquet's theory (modulo shifts) constitute another interesting problem that is worth addressing. The systematic analysis of stability of moving breathers is a challenging task left for future work. It is important to note that this task would only be accessible by standard methods when the velocity and frequency of the traveling breather satisfy specific commensurability conditions. (See, for example, Refs. [57,67] for a relevant discussion.)

In a series of papers, Cuevas *et al.* [19–22] demonstrated that the speed and the orbital stability of the forward DB in DNA can be modified by the LRI. However, their procedure to construct the numerically exact DB involves a selection of an initial condition that is not easy to choose, while in the present study the semidiscrete solution, which is analytically tractable, is selected as the initial guess and further corrected numerically.

The direct usage of the semidiscrete solution in the simulation shows that there are some radiation losses due because the quasicontinuum waves try to adapt to the real system, which is discrete. Furthermore, the continuum limit and multiscale approximation narrow the existence domain of DBs to solutions that have frequencies close to the linear band [1–4]. Floquet's stability analysis of the semidiscrete solution (results not shown in the text) shows that it is always less

stable than the exact DB. In the study of Dauxois *et al.* [37], the same problem was already pointed out during numerical simulations of the short-range Peyrard-Bishop (PB) model. A semianalytical approach similar to what was adopted in a physical setup such as short-range interacting nonlinear left-handed electrical lines and granular materials [38–40] is employed as an attempt to overcome the weakness in this study.

In the PB model, the existence of DBs has been demonstrated [27,28], and DBs are thought to be the precursors to the bubbles that appear before the transcription processes in which large fluctuations of energy have been experimentally observed. The PB model was further amended in order to incorporate the effect of LRI [19–24]. Such interaction was reported to influence the breather, shape, speed, and stability [19–24]. Inspired by the anharmonic model suggested by PB, Joyeux and Buyukdagli (JB) proposed a new model based on site-specific enthalpy and closer to the statistical models [29,30]. This study accounted for LRI as in Refs. [19–24], but highlighted instead the existence of two different regimes, namely forward and backward discrete ILMs, as well as their stability based on the JB model.

The moving breather evidenced in the original DNA model of Peyrard and Bishop was proven to accurately mimic the breathing mode between base pairs as well as the low amplitude breathing modes moving along the molecule, which can be amplified and initiate the transcription process [27]. It is well known that the DNA transcription can be done in two directions. However, the solution obtained from the original PB model cannot explain why this breathing can move backward or forward solely on model parameter values. The incorporation of the long-range interaction in this study was an attempt to address this issue.

The core model used here has been proposed by JB to explain homogeneous/inhomogeneous DNA denaturation and finite stacking enthalpy energy of base pairs [29,30]. This advocates that our results obtained by amending the JB model with LRI can be useful to explore some properties of DNA chains. It is worthwhile to recall that hydrogen bonds responsible for the interbase coupling, namely the hydrogen bond in the N-H$\cdots$O group, is characterized by a finite dipole moment. Therefore, a stretching of the base pair will cause a change of the dipole moment, so that the excitation transfer in the molecule will be due to transition dipole-dipole interaction with a $\mathbf{1}/r^{3}$ dependence on the distance, r. It is also demonstrated that hydrogen-bonded water filaments are linked with nucleotides in DNA [68–70]. In this case, an effective long-range excitation transfer may occur due to the nucleotide-water coupling. The propagating soliton along the DNA molecule was suggested to cause long-range interference with the DNA-protein interaction [28]. These factors can thus modify LRI and breather mobility to corner the energy at the different sites of the DNA. It can therefore foster/enhance the transcription bubble occurrence/amplitude [27,28]. These trapped ILMs may therefore operate as local energy pools and can reassign this encapsulated energy to a localized and propagating transcription bubble. The results obtained in the present study suggest that a suitable balance between the effect of these external factors can prevent amplitude rise and control the spatiotemporal dynamics of the energy.

The transcription of DNA into RNA is not a one-way process: the DNA strand can be read in both directions. One strand of DNA is not identical in one way or another. Indeed, by the structure of the nucleotides that constitute it, there are two types of ends, denoted 5' and 3'. These numbers refer to the carbon numbers of deoxyribose (the DNA D), one of the nucleotide elements. In other words, at the 5' (or 3') end of a strand, it is the 5' carbon (3') of the deoxyribose that is free. Transcription takes place in both directions, 3' to 5', but also 5' to 3' [71]. The directions of transcription processes are different not only for DNA molecules of different living organisms but also for different promoter regions of the same DNA molecule. For some promoters (regions of DNA that lead to initiation of transcription of a particular gene), the transcription process preferably develops in the upstream direction, while for others the process develops in the downstream direction. There are also promoters that do not have a preferred direction of transcription [28].

From the PB model [26–28], or from its improved version [29–35], the dynamical equations have been studied numerically, and a kinklike/breather solution was used as an initial condition. As a result, it was found that an initially static soliton can remain static, oscillate, or move. It can move along the DNA molecule in one of two possible directions (due to an appropriate "kick" or velocity sign of the initial solution): upstream or downstream. In the present study, it is demonstrated that these three events can happen only due to the specific values of the LRI. Note that the direction of transcription further depends on the sequence of bases near the starting point, as well as on the relative position of the initial soliton and the promoter region [72].

V. CONCLUSION

On the theoretical side, in the present study we used the NLS reduction to illustrate the existence of a small-amplitude forward and backward breather arising from the interplay between long-range interactions and the carrier wave frequency. It was further demonstrated that there exist zero-velocity breathers due to the LRI even if the wave number is neither at the edge nor at the center of the first Brillouin zone

Contrary to earlier works that simply tested the robustness of such states with only the use of direct numerical simulations, here we went a significant step further. The numerically discrete exact solutions were identified and continued parametrically over the frequency and LRI values. This allowed us to identify a possible relationship between the discrete breather frequency and the LRI. Their spectral stability was also verified. The mobile discrete breathers are obtained after "kicking" the static discrete breather despite considerable radiation losses due to resonance with phonons.

As highlighted previously, there are nontrivial technical obstacles to overcome toward a calculation for general parameter values of both the frequency and the velocity of the exact traveling discrete breather [57,67]. A numerical study of the stability of periodic traveling and standing waves going beyond the nonlinear Schrödinger solution (NLS) approximation used in this study will also be of interest in order to classify the parameter regimes leading to modulated periodic waves, localized structures, or disordered regimes.

We have demonstrated that bright breathers are not only interesting nonlinear excitations of the DNA model from a theoretical point of view, but they are also within the reach of real word importance for this biopolymer, given the ability to control LRI (e.g., with water solvent). The forward and backward breather could explain the mechanism by which the DNA breathing mode and DNA transcription can be achieved in two directions along the biomolecule.

ACKNOWLEDGMENTS

The authors gratefully acknowledge the advice and support from Juan Francisco Rodríguez Archilla at Universidad de Sevilla, Spain. Thanks to the Electronic Journal Delivery Service of the International Centre of Theoretical Physics (ICTP) for providing valuable references used in this study. We thank the anonymous reviewers for their thorough review and invaluable comments, which improved this paper significantly.

[1] D. K. Campbell, S. Flach, and Y. S. Kivshar, Localizing energy through nonlinearity and discreteness, Phys. Today **57**, 43 (2004).

[2] S. Flach and C. R. Willis, Discrete breathers, Phys. Rep. **295**, 181 (1998).

[3] S. Flach and A. V. Gorbach, Discrete breathers: Advances in theory and applications, Phys. Rep. **467**, 1 (2008).

[4] D. K. Campbell, Fresh breather, Nature (London) **432**, 455 (2004).

[5] S. Aubry and T. Cretegny, Mobility and reactivity of discrete breathers, Phys. D **119**, 34 (1998).

[6] D. Chen, S. Aubry, and G. P. Tsironis, Breather Mobility in Discrete Nonlinear Lattices, Phys. Rev. Lett. **77**, 4776 (1996).

[7] J. D. T. Tchameu, C. Tchawoua, and A. B. Togueu Motcheyo, Effects of next-nearest-neighbor interactions on discrete multibreathers corresponding to Davydov model with saturable nonlinearities, Phys. Lett. A **379**, 2984 (2015).

[8] B. Tang and K. Deng, Discrete breathers and modulational instability in a discrete Φ^4 nonlinear lattice with next-nearest-neighbor couplings, Nonlin. Dyn. **88**, 2417 (2017).

[9] X-L. Chen, S. Abdoulkary, P. G. Kevrekidis, and L. Q. English, Resonant localized modes in electrical lattices with second-neighbor coupling, Phys. Rev. E **98**, 052201 (2018).

[10] G. Miloshevich, J. P. Nguenang, T. Dauxois, R. Khomeriki, and S. Ruffo, Traveling solitons in long-range oscillator chains, J. Phys. A **50**, 12LT02 (2017).

[11] J. E. Macias-Diaz and A. Bountis, Supratransmission in β-Fermi-Pasta-Ulam chains with different ranges of interactions, Commun. Nonlin. Sci. Numer. Simul. **63**, 307 (2018).

[12] Y. Y. Yamaguchi and Y. Doi, Low-frequency discrete breathers in long-range systems without on-site potential, Phys. Rev. E **97**, 062218 (2018).

[13] Y. Yatsuyanagi, Y. Kiwamoto, T. Ebisuzaki, T. Hatori, and T. Kato, Simulations of diocotron instability using a special-purpose computer, MDGRAPE-2, Phys. Plasmas **10**, 3188 (2003).

[14] Y. Kawai, Y. Kiwamoto, K. Ito, A. Sanpei, Y. Soga, J. Aoki *et al.*, Relaxation of azimuthal flow pattern from ring to bell shape through two-dimensional turbulence triggered by diocotron instability, J. Phys. Soc. Jpn. **75**, 104502 (2006).

[15] S. F. Mingaleev and Y. S. Kivshar, Nonlinear transmission and light localization in photonic-crystal waveguides, J. Opt. Soc. Am. B **19**, 2241 (2002).

[16] S. F. Mingaleev, Y. S. Kivshar, and R. A. Sammut, Long-range interaction and nonlinear localized modes in photonic crystal waveguides, Phys. Rev. E **62**, 5777 (2000).

[17] T. Watanabe, T. Iwayama, and H. Fujisaka, Scaling law for coherent vortices in decaying drift Rossby wave turbulence, Phys. Rev. E **57**, 1636 (1998).

[18] M. Molerón, C. Chong, A. J. Martínez, M. A. Porter, P. G. Kevrekidis, and C. Daraio, Nonlinear excitations in magnetic lattices with long-range-interactions, New J. Phys. **21**, 063032 (2019).

[19] J. Cuevas, F. Palmero, J. F. Archilla, and F. Romero, Moving breathers in a bent DNA model, Phys. Lett. A **299**, 221 (2002).

[20] J. Cuevas, J. F. R. Archilla, Y. B. Gaididei, and F. R. Romero, Moving breathers in a DNA model with competing short-and long-range dispersive interactions, Phys. D **163**, 106 (2002).

[21] J. Cuevas, E. B. Starikov, J. F. R. Archilla, and D. Henning, Moving breathers in bent DNA with realistic parameters, Mod. Phys. Lett. B **18**, 1319 (2004).

[22] A. Alvarez, F. R. Romero, J. F. R. Archilla, J. Cuevas, and P. V. Larsen, Breather trapping and breather transmission in a DNA model with an interface, Eur. Phys. J. B **51**, 119 (2006).

[23] J. B. Okaly, A. Mvogo, R. L. Woulaché, and T. C. Kofane, Nonlinear dynamics of damped DNA systems with long-range interactions, Commun. Nonlin. Sci. Numer. Simul. **55**, 183 (2018).

[24] S. F. Mingaleev, P. L. Christiansen, Y. B. Gaididei, M. Johansson, and K. Rasmussen, Models for energy and charge transport and storage in biomolecules, J. Biol. Phys. **25**, 41 (1999).

[25] J. F. R. Archilla, P. L. Christiansen, and Y. B. Gaididei, Interplay of nonlinearity and geometry in a DNA-related, Klein-Gordon model with long-range dipole-dipole interaction, Phys. Rev. E **65**, 016609 (2001).

[26] M. Peyrard and A. R. Bishop, Statistical Mechanics of a Nonlinear Model for DNA Denaturation, Phys. Rev. Lett. **62**, 2755 (1989).

[27] M. Peyrard, Nonlinear dynamics and statistical physics of DNA, Nonlinearity **17**, R1 (2004).

[28] L. Yakusevich, *Nonlinear Physics of DNA, Wiley Series in Nonlinear Sciences* (Wiley, Weinheim, Germany, 2004).

[29] M. Joyeux and S. Buyukdagli, Dynamical model based on finite stacking enthalpies for homogeneous and inhomogeneous DNA thermal denaturation, Phys. Rev. E **72**, 051902 (2005).

[30] M. Joyeux and A-M. Florescu, Dynamical versus statistical mesoscopic models for DNA denaturation, J. Phys.: Condens. Matter **21**, 034101 (2009).

[31] D. Toko, C. B. Tabi, A. Mohamadou, and T. C. Kofane, Coherent modes and parameter selection in DNA models with finite stacking enthalpy, J. Comput. Theor. Nanosci. **9**, 97 (2012).

[32] P. B. Ndjoko, J. M. Bilbault, S. Binczak, and T. C. Kofane, Compact-envelope bright solitary wave in a DNA double strand, Phys. Rev. E **85**, 011916 (2012).

[33] A. Mvogo and T. C. Kofane, Fractional formalism to DNA chain and impact of the fractional order on breather dynamics, Chaos **26**, 123120 (2016).

[34] C. L. Gninzanlong, F. T. Ndjomatchoua, and C. Tchawoua, Discrete breathers dynamic in a model for DNA chain with a finite stacking enthalpy, Chaos **28**, 043105 (2018).

[35] C. L. Gninzanlong, F. T. Ndjomatchoua, and C. Tchawoua, Taming intrinsic localized modes in a DNA lattice with damping, external force, and inhomogeneity, Phys. Rev. E **99**, 052210 (2019).

[36] M. Peyrard, Melting the double helix, Nat. Phys. **2**, 13 (2006).

[37] T. Dauxois, M. Peyrard, and C. R. Willis, Localized breather-like solution in a discrete Klein-Gordon model and application to DNA, Phys. D **57**, 267 (1992).

[38] V. Koukouloyannis, P. G. Kevrekidis, G. P. Veldes, D. J. Frantzeskakis, D. DiMarzio, X. Lan *et al.*, Bright breathers in nonlinear left-handed metamaterial lattices, Phys. Scr. **93**, 025202 (2018).

[39] C. Chong, P. G. Kevrekidis, G. Theocharis, and C. Daraio, Dark breathers in granular crystals, Phys. Rev. E **87**, 042202 (2013).

[40] L. Liu, G. James, P. Kevrekidis, and A. Vainchtein, Breathers in a locally resonant granular chain with precompression, Phys. D **331**, 27 (2016).

[41] S. Flach, Breathers on lattices with long range interaction, Phys. Rev. E **58**, R4116 (1998).

[42] A. V. Gorbach and S. Flach, Compactlike discrete breathers in systems with nonlinear and nonlocal dispersive terms, Phys. Rev. E **72**, 056607 (2005).

[43] S. Abdoulkary, L. Q. English, and A. Mohamadou, Envelope solitons in a left-handed nonlinear transmission line with Josephson junction, Chaos Solitons Fractals **85**, 44 (2016).

[44] Y. Shen, P. G. Kevrekidis, G. P. Veldes, D. J. Frantzeskakis, D. DiMarzio, X. Lan, and V. Radisic, From solitons to rogue waves in nonlinear left-handed metamaterials, Phys. Rev. E **95**, 032223 (2017).

[45] G. P. Veldes, J. Cuevas, P. G. Kevrekidis, and D. J. Frantzeskakis, Quasidiscrete microwave solitons in a split-ring-resonator-based left-handed coplanar waveguide, Phys. Rev. E **83**, 046608 (2011).

[46] A. B. Togueu Motcheyo, J. D. Tchinang Tchameu, S. I. Fewo, C. Tchawoua, and T. C. Kofane, Chameleon's behavior of modulable nonlinear electrical transmission line, Commun. Nonlin. Sci. Numer. Simul. **53**, 22 (2017).

[47] C. Tchawoua, T. C. Kofane, and A. S. Bokosah, Dynamics of solitary waves in diatomic chains with long-range Kac-Baker interactions, J. Phys. A **26**, 6477 (1993).

[48] M. Remoissenet and N. Flytzanis, Solitons in anharmonic chains with long-range interactions, J. Phys. C **18**, 1573 (1985).

[49] T. Dauxois, M. Peyrard, and A. R. Bishop, Entropy-driven DNA denaturation, Phys. Rev. E **47**, R44 (1993).

[50] L. Brillouin, *Periodic Structure: Electronic Filters and Crystal Lattices*, 1st ed. (McGraw-Hill, New York, 1946).

[51] G. P. Veldes, J. Cuevas, P. G. Kevrekidis, and D. J. Frantzeskakis, Coupled backward- and forward-propagating solitons in a composite right- and left-handed transmission line, Phys. Rev. E **88**, 013203 (2013).

[52] T. Yoshinaga, N. Sugimoto, and T. Kakutani, Nonlinear wave interactions on a discrete transmission line, J. Phys. Soc. Jpn. **50**, 2122 (1981).

[53] M. Remoissenet, Low-amplitude breather and envelope solitons in quasi-one-dimensional physical models, Phys. Rev. B **33**, 2386 (1986).

[54] M. Remoissenet, *Waves Called Solitons* (Springer, Berlin, 1994).

[55] *The Nonlinear Schrödinger Equation: Self-Focusing and Wave Collapse*, edited by C. Sulem and P-L. Sulem (Springer, New York, 2004).

[56] G. Fibich, *The Nonlinear Schrödinger Equation* (Springer International, Cham, 2015).

[57] J. F. R. Archilla, Y. Doi, and M. Kimura, Pterobreathers in a model for a layered crystal with realistic potentials: Exact moving breathers in a moving frame, Phys. Rev. E **100**, 022206 (2019).

[58] M. Sato, T. Nakaguchi, T. Ishikawa, S. Shige, Y. Soga, Y. Doi, and A. J. Sievers, Supertransmission channel for an intrinsic localized mode in a one-dimensional nonlinear physical lattice, Chaos **25**, 103122 (2015).

[59] J. L. Marín and S. Aubry, Breathers in nonlinear lattices: numerical calculation from the anticontinuous limit, Nonlinearity **9**, 1501 (1996).

[60] A. Alvarez, F. R. Romero, J. Cuevas, and J. F. R. Archilla, Phys. Lett. A **372**, 1256 (2008).

[61] R. Morandotti, H. S. Eisenberg, Y. Silberberg, M. Sorel, and J. S. Aitchison, Self-Focusing and Defocusing in Waveguide Arrays, Phys. Rev. Lett. **86**, 3296 (2001).

[62] F. T. Ndjomatchoua, C. Tchawoua, J. D. T. Tchinang, B. P. LeRü, and H. E. Z. Tonnang, Discrete Davydovâs soliton in α-helical protein molecule with anharmonic hydrogen bond and thermal noise, Commun. Nonlin. Sci. Numer. Simul. **29**, 148 (2015).

[63] F. T. Ndjomatchoua, C. Tchawoua, F. M. M. Kakmeni, B. P. LeRü, and H. E. Z. Tonnang, Waves transmission and amplification in an electrical model of microtubules, Chaos **26**, 053111 (2016).

[64] T. Misawa, N. Ohno, K. Asano, M. Sawai, S. Takamura, and P. K. Kaw, Experimental Observation of Vertically Polarized Transverse Dust-Lattice Wave Propagating in a One-Dimensional Strongly Coupled Dust Chain, Phys. Rev. Lett. **86**, 1219 (2001).

[65] A. B. Togueu Motcheyo, E. Nkendji Kenkeu, J. Djako, and C. Tchawoua, Backward-wave propagation with vertical dust grain oscillations in dusty plasma crystals, Phys. Plasmas **25**, 123701 (2018).

[66] V. G. Veselago, The electrodynamics of substances with simultaneously negative values of ϵ and μ, Sov. Phys. Usp. **10**, 509 (1968).

[67] J. Gómez-Gardeñes, F. Falo, and L. M. Floría, Mobile localization in nonlinear Schrödinger lattices, Phys. Lett. A **332**, 213 (2004).

[68] D. C. Rau and V. A. Parsegian, Direct measurement of the intermolecular forces between counterion-condensed DNA double helices. Evidence for long range attractive hydration forces, Biophys. J. **61**, 246 (1992).

[69] G. Corongiu and E. Clementi, Simulations of the solvent structure for macromolecules. I. Solvation of B-DNA double helix at T = 300 K, Biopolymers **20**, 551 (1981).

[70] U. Dahlborg and A. Rupprecht, Hydration of DNA: A neutron scattering study of oriented NaDNA, Biopolymers **10**, 849 (1971).

[71] P. Raven, G. Johnson, K. Mason, J. Losos, and S. Singer, *Biology*, 11th ed. (McGraw-Hill, New York, 2017).

[72] M. Salerno, Discrete model for DNA-promoter dynamics, Phys. Rev. A **44**, 5292 (1991).